# Direct Simulation of Magnetic Resonance Relaxation Rates and Line Shapes from Molecular Trajectories

David P. Rangel,*,[†,§] Philippe C. Baveye,[‡] and Bruce H. Robinson[†]

[†]Department of Chemistry, University of Washington, Seattle, Washington 98195, United States
[‡]Department of Civil and Environmental Engineering, Rensselaer Polytechnic Institute, Troy, New York 12180, United States

ABSTRACT: We simulate spin relaxation processes, which may be measured by either continuous wave or pulsed magnetic resonance techniques, using trajectory-based simulation methodologies. The spin–lattice relaxation rates are extracted numerically from the relaxation simulations. The rates obtained from the numerical fitting of the relaxation curves are compared to those obtained by direct simulation from the relaxation Bloch–Wangsness–Abragam–Redfield theory (BWART). We have restricted our study to anisotropic rigid-body rotational processes, and to the chemical shift anisotropy (CSA) and a single spin–spin dipolar (END) coupling mechanisms. Examples using electron paramagnetic resonance (EPR) nitroxide and nuclear magnetic resonance (NMR) deuterium quadrupolar systems are provided. The objective is to compare those rates obtained by numerical simulations with the rates obtained by BWART. There is excellent agreement between the simulated and BWART rates for a Hamiltonian describing a single spin (an electron) interacting with the bath through the chemical shift anisotropy (CSA) mechanism undergoing anisotropic rotational diffusion. In contrast, when the Hamiltonian contains both the chemical shift anisotropy (CSA) and the spin–spin dipolar (END) mechanisms, the decay rate of a single exponential fit of the simulated spin–lattice relaxation rate is up to a factor of 0.2 smaller than that predicted by BWART. When the relaxation curves are fit to a double exponential, the slow and fast rates extracted from the decay curves bound the BWART prediction. An extended BWART theory, in the literature, includes the need for multiple relaxation rates and indicates that the multiexponential decay is due to the combined effects of direct and cross-relaxation mechanisms.
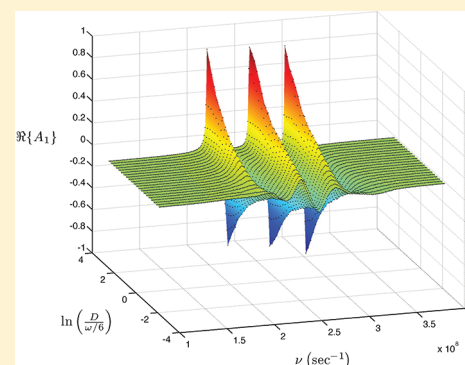
1. INTRODUCTION

Magnetic resonance (MR) techniques provide sensitive measures of the collective and internal dynamics of molecular systems across a wide range of time scales. In particular, electron paramagnetic resonance (EPR) is a powerful technique that can be used to measure rotational correlation times ranging from picoseconds to milliseconds.[1−3] The site-directed spin-labeling (SDSL) methodology[4−6] has enabled researchers to use EPR to examine dynamics processes in many biological arenas.[4−8] Spectral widths due to spin–spin relaxation (R_{2e}) and spin–lattice relaxation rates (R_{1e}), as obtained in continuous-wave (CW) and time-domain (TD) EPR, provide a sensitive measure of motions of spin-labels and molecular systems.[4−6,9−11] For example, MR methods have been used to study the effect of clay particle surfaces on water structuring by detecting decreased mobility of spin probes.[12] In studies involving EPR imaging, the collapse of radical-containing nanoparticles during pH titration can be observed as a shift from hindered to unhindered rotation.[13]

Line shape simulation methods[9,10,14] and relaxation rate analysis[11,15] have made it possible to obtain quantitative measures of system dynamics. In MR relaxation studies, the effects of dynamics are generally analyzed through Bloch–Wangsness–Abragam–Redfield theory (BWART)[3,16,17] and

often use simplified or general motional models[11,17] and "model free" approaches to extract characteristic rates of motion.[18]

The direct conversion of arbitrarily complex dynamics of a system into MR spectra is known as the "trajectory-based" method and has been of considerable interest to a large community for several decades.[19−24] The fundamental equation of motion of the spin observables relies on the Kubo–Tomita theory (KTT)[25] that shows how to separate the spin-system dynamics from the molecular dynamics (MD), and provides an equation for spin-system evolution and equilibrium. The arbitrarily complex motions that can be simulated using MD do not lend themselves to simple models parametrizing the trajectories, as has been demonstrated by Håkansson et al.[26] However both CW spin line shape and relaxation rates can be calculated from the trajectories.

The trajectory method is computationally more intensive than simulations based on either BWART, with analytically derived expressions for relaxation rates, or line shape

simulations using the stochastic Liouville equation (SLE). However, the trajectory method is computationally competitive with numerically based BWART simulations in which the underlying molecular trajectories are used to calculate relaxation rates. The availability of inexpensive and powerful computers has increased interest in the trajectory-based method.[26−37] Moreover, because it is computationally intensive to generate MD-based trajectories, one expects the incremental time needed to generate spectral responses to be small enough to warrant developing methods that, while also computer intensive, demonstrate the principle that spectra can be generated from trajectory information alone. Oganesyan[31] has recently reported a method for generating EPR spectra from truncated dynamical trajectories that reduces the computational demands and increases the feasibility of the direct simulation approach.

Methods are now well-established that demonstrate that MD trajectories can be faithfully transformed into both relaxation rates and CW line shapes.[26,28,29,31,33] Of course the trajectories must be sampled often enough to cover the time scale implicit in the Hamiltonian and of sufficient length to obtain converged simulations.[27,34] Trajectory methods have been used to obtain CW spectra by either directly simulating the line widths from the trajectories or merely including a phenomenological relaxation rate that approximates the appropriate line width.[34] Approaches that use MD-based trajectories efficiently and even combine trajectories on the picosecond time scale with Markovian dynamics at longer time scales show promise.[34,38] In particular, in addition to simulating CW spectra, Håkansson et al.[26] numerically calculate the Redfield spin−spin relaxation matrix element by calculating the spectral densities in that element from MD trajectories. Oganesyan[31] has shown that the relaxation rates could be generated from first principles, and others have included experimentally determined line widths that are added to the simulation to account for additional relaxation.[22,34,36,39]

Our primary focus in this paper is to determine the spin−lattice relaxation rate using the trajectory-based methods wherein relaxation rates are obtained from the trajectory-based methods directly from the relaxation of the observables by data fitting. Herein, rates, determined by exponential fitting to the observable's relaxation, are compared with BWART rates generated numerically from the underlying correlation functions and with rates calculated from the analytic forms from BWART, which are often used to relate relaxation rates and rigid body motion. In this study we have restricted the motion of the spin-label to anisotropic rigid body motion so that the comparison between numerical and analytical methods becomes more transparent.

Throughout the studies presented below, the Hamiltonians of the equations of motion are not partitioned into secular, pseudosecular, and nonsecular portions. Instead, all components of the relevant bilinear Hamiltonians are used to evolve the system, as others have done recently.[26,31,34,40] In the methods used in this work, the code autonomously converts the equations from Hamilton to Liouville space wherein the density matrix is replaced by a vector containing the set of measurable MR observables. The conversion uses the spherical tensor formalism applied to MR relaxation as presented by Nielsen et al.[11,41] Coherence and relaxation both appear in the MR observables under a single (complete) Hamiltonian.

We have neglected several relaxation mechanisms in this study which are important to simulate accurate CW MR line shapes.[9,10] In particular, the effects of the spin-rotation mechanism[42] and oxygen relaxation are neglected.[10,43] Additional inhomogeneous broadening mechanisms, primarily due to the presence of many weakly coupled protons, are also neglected. As these issues have been dealt with by others[22,26,29,34,36,39] and our focus is *not* on simulating experimental line shapes but rather on comparisons of spin−lattice relaxation among simulation methods, we do not pursue these additional features in this paper.

In the following, we simulate EPR relaxation rates for several spin systems using the electron−nuclear dipolar coupling (END) and chemical shift anisotropy (CSA) Hamiltonians at 250 MHz via the two trajectory-based methods and compare the results with analytic BWART predictions for spin−spin and spin−lattice relaxation. Our focus is primarily on the spin−lattice relaxation rate, and therefore, we choose motional times that cover the range where the CSA and END mechanisms are most active. Simple BWART makes clear this will happen when the diffusion rates are on the order of the observer frequency. Thus, the diffusion rates are presented relative to the observer frequency. We used the same time range as well when obtaining spin−lattice relaxation rates. Therefore the spin−lattice relaxation rates (and corresponding CW spectra) go from the fast to the intermediate-motion range. Representative CW spectra, obtained from the simulated S_+ observable, using the Zeeman-filtered spectral transform method[44] are shown to illustrate the connection between the spin−lattice relaxation rates and the spectral shapes. The 250 MHz spectral frequency used in this work is important in its own right,[45] and is relevant in EPR imaging.[46−48] In addition to simulations of EPR relaxation rates and line shapes, we simulate deuterium quadrupolar nuclear magnetic resonance (^{2}H NMR, or DQR) spectra. The quadrupolar tensor operator used in deuterium NMR is bilinear in form and contains the dependence on molecular orientation that is modified by molecular trajectories. The results constitute a benchmark with which to test the accuracy of the rates predicted by both the trajectory-based methods and BWART because, for simple motional processes, agreement between the methods is an essential first step. As the motional processes become more complex, the MR response functions and relaxation rates simulated using molecular trajectory methods must be considered to be more complete.

2. THEORY

2.1. Equations of Motion. The fundamental equation of motion governing the evolution of the spin system coupled to a lattice bath is[11,25,49]

$$\frac{d\Delta\rho}{dt} = -i[H, \Delta\rho] - i[H_\omega, \rho] \tag{2.1}$$

where $\Delta\rho$ is the difference of the complete spin density matrix, ρ, and the equilibrium spin density matrix, ρ_{eq}. In eq 2.1, H is the Hamiltonian for both the spin system and the spin−lattice coupling. It includes terms that are nonstationary in the rotating frame. However, it contains no purely lattice terms. All of the effects of the lattice are transmitted to the Hamiltonian by molecular dynamical processes and through the equilibrium spin density matrix.[25,41] H_ω is a coherent driving Hamiltonian that includes a time-varying external light field acting on the spin system. H operates only on the

difference density matrix, $\Delta\rho$; if H operates on ρ itself, the net magnetization is driven to zero by relaxation processes following a perturbation. H_ω must operate on the total density matrix, ρ, in order to drive the spin system away from equilibrium; the net magnetization calculated from $\Delta\rho$ fluctuates about zero, and cannot be rotated by the perturbation Hamiltonian H_ω.

In this work, any bilinear spin Hamiltonian can be used in the simulations. In particular, H combines the chemical shift anisotropy (CSA), electron−nuclear dipolar (END), and quadrupolar effects:

$$H(t) = -\gamma_e B G_e(t) S + \gamma_n B G_n(t) I_n + I_n A(t) S + \gamma_q B G_q(t) I_q$$
$$+ q I_q Q(t) I_q \qquad (2.2)$$

where B is the applied Zeeman field (generally in the z direction), S is the spin operator of the electron, I_n is the spin operator of the nucleus coupled to S, and I_q is the nuclear spin operator of a quadrupolar nucleus. G_q, G_e and G_n are the chemical shift anisotropy tensors of the quadrupolar nucleus, electron, and electron-coupled nucleus, respectively. The G tensors couple the spins to the external field, B. G_e contains the spin−orbital contribution to the Hamiltonian. A is the electron−nuclear dipolar tensor. A contains both the dipolar and contact electron−nuclear interaction terms.[50] Q is the nuclear quadrupolar tensor, and q is the strength of the interaction. γ_q, γ_e and γ_n are the gyromagnetic ratios for the quadrupolar nucleus, electron, and electron-coupled nucleus, respectively. Generally, the quadrupolar nucleus, such as deuterium, is not coupled to another spin, but is permitted to do so in the above formalism. Also, there is nothing in the formalism to distinguish between an electronic spin and a nuclear spin; the use of the symbol I for nuclei and S for electrons in the Hamiltonian above is for clarity. Not all the terms in eq 2.2 will be included simultaneously in each of the simulations considered below.

The time dependence in the coupling tensors (G_e, G_n, A, and Q) is due to their anisotropy and the underlying physical rotation of the molecular frame to which the spins are attached. The molecule generates a reorientation process that rotates the principal axial coordinate system (PAS) in which the tensors are diagonal. In addition, the interspin distance can be dynamically changed. The underlying dynamics of the spin probe are referred to as molecular trajectories in what follows, whereas the spin system evolves in response to the rotational dynamics under the action of the Hamiltonian. The time dependence in each bilinear term in H can be made explicit by incorporating the rotation matrix obtained from trajectories into the Hamiltonian. The molecular trajectory creates time dependence in the Hamiltonian through the rotation, $\Omega(t)$, from the lab frame to the PAS of the A and G tensors. The A and G tensors do not need to be codiagonal, and there can exist an arbitrary (constant) rotation between these two frames. For example, the Hamiltonian governing the CSA mechanism, with frames of reference explicitly indicated, can be written using Cartesian rotation matrices, $R(t)$ as

$$H_e^{CSA}(t) = -\gamma_e B^{lab\dagger} R_{LG}^\dagger(t) G_e^{PAS} R_{LG}(t) S^{lab} \qquad (2.3)$$

where $R_{LG}(t)$ is the rotation from the lab reference frame of the classical magnetic field operator B and the quantum spin operator S to the principal axial system in which the G_e

tensor is diagonal, or rotated by a fixed amount. The time dependence appears in the END and quadrupolar Hamiltonians in precisely the same manner. Additionally, internuclear distances can evolve, the effects of which can be incorporated into a distance-dependent strength of the interaction tensors. In the simulations, rotations are carried out in Cartesian space, rather than using the spherical Wigner rotation matrices, $D^{(1)}(\Omega(t))$.

The coherent driving Hamiltonian in eq 2.1 is due to a time-varying external field interacting with electrons and nuclei via the CSA mechanism. The Hamiltonian takes the form

$$H_\omega(t) = -\gamma_e B_\omega(t)\, G_e(t) S + \gamma_n B_\omega(t)\, G_n(t) I_n \qquad (2.4)$$

Because of fluctuations in G_e and G_n, H_ω is not strictly coherent. There will be relaxation effects that contribute to the return of the system to equilibrium.[3] In this work, these additional relaxation mechanisms are ignored due to the short duration of the applied coherent field during $\pi/2$ pulses used to drive the system away from equilibrium.

The conversion from Cartesian operators appearing in the Hamiltonians to spherical tensor operators, $\hat{T}_q^k$, is carried out by the program automatically as discussed in Appendix C. The result of the conversion is an equation of motion recast in Liouville space. In the spherical tensor formalism,[49] the equation of motion for the magnetic resonance observables is given by

$$\frac{d\Delta O}{dt} = -iL(t)\Delta O - iL_\omega(t)O \qquad (2.5)$$

where L and L_ω are the Liouville representations of H and H_ω, respectively. O and ΔO are the spherical-tensor spin-operator observables and difference observables, respectively. The construction of this spherical tensor observable version of the equation of motion has been published elsewhere,[49] and a review of the relevant portions of the theory is presented in Appendix C. The elements of O are given by $O_q^k = \text{tr}\{\hat{T}_q^k \rho\}$. The vectorial indices on the unit spherical tensors, $\binom{k}{q}$, account for ordered Kronecker products of spin operators in multispin systems (see Appendix C). $\Delta O \equiv O - O_{eq}$ is the vector of deviations of the observables from their equilibrium values, $O_{eq} \equiv O_{\rho_0}$. The individual equilibrium observables are calculated by using the equilibrium density matrix, ρ_0; $O_{\rho_0 q}^{\ \ k} = \text{tr}\{\hat{T}_q^k \rho_0\}$. The equilibrium density matrix is given by $\rho_0 = e^{-\beta\bar{H}}/\text{tr}\{e^{-\beta\bar{H}}\}$, where $\bar{H}$ is the time-independent Hamiltonian of the system, calculated numerically as the average over long trajectories, or approximated by a stationary Hamiltonian that approximates $\bar{H}$.

The Hamiltonians appearing in eq 2.1 are written in the Liouville representation in which $L = \sum_{k,q} H_q^k \mathcal{L}_q^k$. Formulas for the $\mathcal{L}$ matrices are available in the literature.[49] The $\mathcal{L}$ matrices for the spin 1/2 system used in one set of simulations (see section 3.1) are given in Table 1. The H_q^k elements are defined in Appendix C and contain the constants necessary to describe specific spin systems. They are obtained from the Cartesian Hamiltonian automatically by the program.

In practice, when a driving field is on, eq 2.5 is rewritten in terms of the evolution of the total observables vector, O, as follows:

Table 1. Spherical Tensor Operators and Liouville Space Operators[49] for a Spin $\nu = 1/2$ System[a]

$$^{(1)}\hat{T}_0^0 = \frac{1}{\sqrt{2}}\begin{pmatrix} 1 & 0 \\ 0 & 1 \end{pmatrix} \qquad ^{(1)}\hat{T}_{-1}^1 = \begin{pmatrix} 1 & 0 \\ 0 & 1 \end{pmatrix}$$

$$^{(1)}\hat{T}_0^1 = \frac{1}{\sqrt{2}}\begin{pmatrix} -1 & 0 \\ 0 & 1 \end{pmatrix} \qquad ^{(1)}\hat{T}_1^1 = \begin{pmatrix} 0 & 0 \\ 1 & 0 \end{pmatrix}$$

where $[^{(j)}\hat{T}_q^k]_{mn} = (-1)^{k+m+j}(2k+1)^{1/2}\begin{pmatrix} j & k & j \\ n & q & -m \end{pmatrix}$ and $j = 2\nu + 1$

$$^{(1)}\mathcal{L}_0^0 = \begin{pmatrix} 0 & 0 & 0 & 0 \\ 0 & 0 & 0 & 0 \\ 0 & 0 & 0 & 0 \\ 0 & 0 & 0 & 0 \end{pmatrix} \qquad ^{(1)}\mathcal{L}_{-1}^1 = \sqrt{2}\begin{pmatrix} 0 & 0 & 0 & 0 \\ 0 & 0 & 0 & 0 \\ 0 & -1 & 0 & 0 \\ 0 & 0 & -1 & 0 \end{pmatrix}$$

$$^{(1)}\mathcal{L}_0^1 = \sqrt{2}\begin{pmatrix} 0 & 0 & 0 & 0 \\ 0 & 1 & 0 & 0 \\ 0 & 0 & 0 & 0 \\ 0 & 0 & 0 & -1 \end{pmatrix} \qquad ^{(1)}\mathcal{L}_1^1 = \sqrt{2}\begin{pmatrix} 0 & 0 & 0 & 0 \\ 0 & 0 & 1 & 0 \\ 0 & 0 & 0 & 1 \\ 0 & 0 & 0 & 0 \end{pmatrix}$$

where $[^{(j)}\mathcal{L}_q^k]_{\binom{k'}{q'}\binom{k''}{q''}} = \text{tr}\{^{(j)}T_{q'}^{k'}[^{(j)}\hat{T}_q^k, \, ^{(j)}\hat{T}_{q''}^{k''}]\}$

[a]Note that the spin index, ν, within the matrices runs from $-\nu$ to ν in integer steps as opposed to the conventional descending order.

$$\frac{dO(t)}{dt} = -i(L(t) + L_\omega(t))O(t) + iL(t)O_{eq} \tag{2.6}$$

This equation is then solved numerically at time steps, τ, that are small compared to any eigenfrequencies of the spin system, and small enough to correctly sample the underlying molecular dynamics. This is accomplished by using the following numerical solution:

$$O(t_0 + \tau) = e^{-i\tau(L(t_0)+L_\omega(t_0))}O(t_0)$$
$$- \tau/2(e^{-ia\tau(L(t_0))} + e^{-ib\tau(L(t_0))})O_{in}(t_0) \tag{2.7}$$

where $a + b = 1$ and $a^2 + b^2 = 2/3$. $O_{in}(t_0) = iL(t_0)O_{eq}$ is the inhomogeneous contribution to the observables from the driving field. For sufficiently small time steps, τ, the approximation in eq 2.7 is exact to third order as discussed in Appendix A. The development of eq 2.7 is one of the major contributions of this paper, because it describes how pulses enter into the equations of motion for the spin system with relaxation coupled to the bath. Equation 2.6 illustrates the principle that the coherent driving term ($L_\omega(t)$) drives the entire magnetization O, whereas stochastically modulated terms in the Hamiltonian drive only the part of the magnetization that deviates from equilibrium. The exponential matrix is calculated using the Padé approximation with scaling and squaring[51−53] as implemented in Matlab (The Mathworks, Natick, MA, USA). When the driving field is switched off, we determine the set of deviations of the observables from their equilibrium values ($\Delta O \equiv O - O_{eq}$)

$$\frac{d\Delta O(t)}{dt} = -iL(t)\,\Delta O(t) \tag{2.8}$$

using the exponential matrix:

$$\Delta O(t_0 + \tau) = e^{-i\tau L(t_0)}\Delta O(t_0) \tag{2.9}$$

In the simulations, the system's initial condition is O_{eq} and a $\pi/2$ pulse is applied to drive the system away from equilibrium.

The driving field is then turned off and the magnetization is allowed to relax back to equilibrium.

In order to relate the results to spectroscopic measurements, the average behavior of the observables for an ensemble of spins in the system must be calculated. We calculate this average by running the evolution of O for many molecular trajectories until we have a sufficiently large signal-to-noise ratio. The result is a trajectory-averaged evolution of the ensemble-averaged observables, $\bar{O}$, which is the classical ensemble average of the observables:

$$\bar{O} = \frac{1}{N}\sum_{n=1}^{N} O \tag{2.10}$$

where N is the total number of trajectories. The Sydney Opera House (SOPHE) method[54] for simulating randomly oriented powder spectra is used to set the initial angles for the N trajectories included in the simulations. This simple partitioning of the unit sphere is relatively efficient at faithfully averaging over the sphere.[55] The accurate sampling of initial orientation plays a more significant role in line shape results as the diffusion rate slows. In this slow motion regime, the mean-squared angular deviation between steps in the molecular trajectories shrinks, and the MR spectrum approaches that of a powder pattern. In such cases, it is essential to properly sample angular orientations of the spin probe.[56−58] The N runs uniformly sample the solid angle of the first octant of the sphere.

The simulations are run in the Cartesian lab-fixed frame using circularly polarized light for $\pi/2$ pulses. Simulation time steps must be short relative to the fastest resonant frequencies of the spin system and the most rapid motions in the underlying molecular system. Proper sampling prevents aliasing of resonant frequencies of the spin system and allows for the proper sampling of high frequency molecular rotations that contribute to relaxation rates and line widths. Because the Hamiltonian includes nonsecular terms, the time scale of the sampling must be rapid with respect to both the diffusion process and the observer frequency. There is no advantage in going into a rotating frame unless one can use a stationary, truncated Hamiltonian.

For comparison of the simulation results, the BWART equation of motion[16] is used to obtain theoretical values for spin−lattice relaxation rates. In BWART, a secular (time-dependent) Hamiltonian for the system is postulated and a coupling to the lattice is added as a perturbation term, which couples the spin system to the molecular or lattice fluctuations. BWART uses this fluctuating lattice term to construct a relaxation rate matrix which replaces the time-dependent coupling Hamiltonian in the final equation. In the spherical tensor formalism,[49] the BWART equation is

$$\frac{d\Delta O}{dt} = -i(L_0 + L_\omega(t))\Delta O - iL_\omega(t)O_{\rho_0}$$
$$- \left(\int_0^\infty \overline{\tilde{L}_f(0)\,\tilde{L}_f(-\tau)}\,d\tau\right)\Delta O \tag{2.11}$$

L_0 is the time- and fluctuation-independent or constant contribution to the total Liouville-space Hamiltonian. $L_f(t)$ represents the stochastically modulated Liouville-space Hamiltonian that couples the lattice or bath variables to the spin system, and $\tilde{L}_f(t - \tau) = e^{iL_0\tau}L_f(t)e^{-iL_0\tau}$. $L_\omega(t)$ is the same driving magnetic field contribution used in eq 2.5. As before, $L_\omega(t)$ operates on the observables vector directly rather on than their deviation from equilibrium.[11,16,41] The first term on the

right-hand side of eq 2.11 represents the evolution of the spin system under a coherent Hamiltonian. The second term is subtracted so that L_ω acts on the vector of observables. Finally, in eq 2.11, the third term on the right-hand side, $\int_0^\infty \widetilde{L_f}(0)\,\widetilde{L_f}(-\tau)\,d\tau$, is known as the BWART relaxation matrix that describes the relaxation of the system to equilibrium. This term will be denoted by R in what follows. In this term, the overline represents ensemble averaging over the degrees of freedom of the system. These degrees of freedom come from the evolution of terms in L_f, and the same processes that drive the rotation of the G, A, and Q tensors in the full equation of motion (see eq 2.5) also drive the fluctuations in L_f. In section 2.2, a numerical method for determining L_f from the total L will be developed. This fluctuating Liouville-space Hamiltonian assumes no particular model for the underlying molecular motion, however, thereby escaping the limited cases for which BWART can provide analytical expressions for R.

Expressions for the $\langle S_z \rangle$ direct spin−lattice relaxation rate, $R_{3,3}$ (equivalent to R_{1e} for the single spin 1/2 system), have been derived previously,[11,15] and are given in Appendix B. The values calculated according to the equations given there are used for comparisons with simulation results. In numerical simulations, the stochastic parts of the total Hamiltonian are *not* removed from the full Hamiltonian; i.e., $L_f(t)$ is never removed from L. By doing so, no assumptions are made about the nature of the secular and nonsecular parts of the Hamiltonian, thereby avoiding some of the limitations of BWART. For example, there is no need to provide an analytical expression for R explicitly, which allows for the inclusion of molecular dynamics of arbitrary complexity on any time scale.

2.2. Numerical Calculation of the Relaxation Matrix. A relaxation term can be incorporated in the simulations, with the relaxation matrix either determined *a priori* (e.g., BWART) or via a more direct, but entirely computational method. The theory presented thus far affords a means to calculate the relaxation matrix, R, from trajectories. The method involves determining the fully stationary part of the Hamiltonian, then determining the remnant fluctuating Hamiltonian. This remainder is used to determine the relaxation matrix numerically as described in the following procedure.

By definition, the time-invariant, ensemble averaged Hamiltonian is the BWART coherent Hamiltonian, H_0, or L_0 in Liouville space. The direct calculation of the average from trajectories is the most direct, numerically based means to ascertain the time-invariant Hamiltonian; in systems with complex underlying dynamics, such a numerical scheme is necessitated by the fact that an analytic expression for the average may not be calculable. Numerically, this operator is calculated from M trajectories, each of which is N time steps long and is denoted as $\bar{L}$:

$$\bar{L} = \frac{1}{MN} \sum_{m=1}^{M} \sum_{n=1}^{N} L_n^{(m)} \tag{2.12}$$

The fluctuating Liouville-space Hamiltonian that drives the relaxation process is then the difference of the averaged Liouville-space Hamiltonian and full Liouville-space Hamiltonian:

$$L_f(t) = L(t) - \bar{L} \tag{2.13}$$

Calculation of the relaxation matrix also requires the calculation of L_f in the interaction frame:

$$\widetilde{L_f}(t) = e^{it\bar{L}} L_f(t) e^{-it\bar{L}} \tag{2.14}$$

With the inclusion of a correlation matrix, C, defined as

$$C(\tau) \equiv \overline{L_f(0)\,\widetilde{L_f}(\tau)} \tag{2.15}$$

where the bar again denotes ensemble averaging, the relaxation matrix can be expressed as

$$R = \int_{t'=0}^{\infty} C(t')\,dt' \tag{2.16}$$

This integral can be approximated as follows:

$$R \approx \sum_{n=1}^{N} \sum_{m=1}^{M} [L_f(0)\,\widetilde{L_f}(t_n)]_m \Delta t \tag{2.17}$$

where the quantity enclosed by brackets, [ ], is an approximation to one member of the ensemble-averaged correlation function, C. Equation 2.17 can be used to calculate the decay of the z magnetization after a pulse, and the results can be compared with direct calculations from the decay in the observable. Equation 2.17 provides an approach to compute *all* elements of the R matrix. Previous calculations of specific elements of importance for CW EPR that are included in this matrix have been carried out and have demonstrated that such calculations lead to reasonable results.[26]

Once calculated, R is incorporated into eqs 2.6 and 2.8. When the driving field is on, the relaxation matrix R is included as a damping term acting on ΔO:

$$\frac{dO}{dt} = -i(\bar{L} + L_\omega - iR)O + i(\bar{L} - iR)O_{eq} \tag{2.18}$$

Once the driving field is removed, the equation used in the simulation is homogeneous:

$$\frac{d\Delta O}{dt} = -i(\bar{L} - iR)\Delta O \tag{2.19}$$

In the simulations conducted in this research, molecular trajectories used to calculate $C(\tau)$ in the fast motion limit had a time step size on the order of 10^{-1} smaller than those used to simulate the observables O in order to adequately sample the rapid decay of $C(\tau)$. For the intermediate and slower motional regimes, the same trajectories used to evolve O may be used since $C(\tau)$ decays on a much longer time scale. Although not performed in this work, it is also possible to calculate the relaxation effects of a CW oscillating field[3] and incorporate this into the calculation of R by including $L_\omega(t)$ in eq 2.7, 2.9, or 2.13.

3. SIMULATIONS AND RESULTS

The spin is governed by various combinations of the CSA, END, and quadrupolar Hamiltonians as expressed in eq 2.2. The magnitude of the magnetic field, B, is chosen so that each of the spin systems considered in the results has a central resonance of 250×10^6 Hz. The G and A tensors are assumed to be diagonal in the molecular frame (MF); i.e., the PAS of the spin system moves with the molecular probe. The underlying molecular motion is then incorporated into a trajectory of G and A tensors through the generation of a time series of rotation matrices that connect the lab to spin coordinate systems. For example, in the case of a nitroxyl CSA−END Hamiltonian

$$H(t) = IA(\Omega(t))S - \gamma_e B G_e(\Omega(t))S + \gamma_n B G_n(\Omega(t))I_n \tag{3.1}$$

For the systems considered here, it has been assumed for simplicity that the A and G tensors are collinear, which is an excellent approximation for spin-labels.[11] There is no loss in generality, however, since any arbitrary relation of A to G is allowed by the theory and requires only a constant rotation to be included in the simulation.

The molecular trajectory is generated using the global rotational diffusion (GRD) method developed previously.[34,59,60] This rapid quaternion-based Monte Carlo (MC) simulation technique is used to generate Brownian trajectories and can simulate a rigid body diffusing with three independent diffusion constants, one about each axis in the MF. The rotational diffusion constants used in the MC trajectories were selected to span the slow to fast motional regimes relative to the resonance frequency of the system. This is the range over which spin–lattice relaxation operators contribute to the spin–lattice relaxation. The range over which these mechanisms provide relaxation can be understood in terms of the analytic theory, which shows that the spectral density functions for spin–lattice relaxation for these mechanisms centers around the spectrometer frequency. In this study, spherically ($D_{xx} = D_{yy} = D_{zz}$) and cylindrically ($D_{yy} = D_{zz} = D_\perp$, $D_{xx} = D_\parallel$) symmetric rigid bodies are used to generate molecular trajectories since there exist analytical expressions for the relaxation rates in BWART. This allows for a comparison of simulation to theory. It is assumed, for simplicity, that the principal axis frame of the diffusion tensor, D, is coincident with the PAS of the G and A tensors[15] and the MF. For spherically symmetric diffusion, the rotational diffusion constants are centered at $D_0 = \omega/6$, where $\omega = 2\pi(250 \times 10^6)$, and vary according to $D = fD_0$, where $f = 10^{n/10}$ and $n = \{-10, -9, ..., -1, 0, 1, ..., 9, 10\}$ in order to span the motional regimes from $D = 0.017\omega$ to $D = 1.6\omega$. For the ^{15}N system discussed below, we also simulated at $n = \{-20, -15\}$ in addition to the other D values listed above. For cylindrically symmetric anisotropic diffusion, $D_{xx} = D_{zz} = fD_{yy}$, where $f = 10^{n/10}$ and $n = \{-10, -9, ..., -1, 0, 1, ..., 9, 10\}$ and $D_{yy} = \omega/6$. The Marsenne twister pseudorandom number generator is used to create the random deviates used in the MC algorithm.[61]

In the simulations, the following observables for the spin 1/2 system are considered:[11,49] (a) $O_3 \equiv O_0^1 \equiv \sqrt{2}\langle S_z \rangle$; (b) $O_4 \equiv O_1^1 \equiv -(\langle S_x \rangle - i\langle S_y \rangle)$; (c) $R_{3,3} \equiv R_{1e} \equiv 1/T_1$, the direct spin–lattice relaxation rate; (d) $R_{4,4} \equiv R_{2e} \equiv 1/T_2$, the direct spin–spin relaxation rate of the electron. All rates are reported in frequency units.

For the coupled electron spin 1/2–nuclear spin 1/2 (e.g., ^{15}N spin-label) and electron spin 1/2–nuclear spin 1 (e.g., ^{14}N spin-label) multispin systems, one has the following:[11,49] (a) $O_3 \equiv O_{0,0}^{1,0} \equiv \sqrt{2}\langle S_z \otimes 1_n \rangle$, i.e., the spin operator for the electron in the combined space of the multispin system where 1_n is the nuclear identity spin operator; (b) $O_4 \equiv O_{1,0}^{1,0} \equiv (\langle S_x \otimes 1_n \rangle - i\langle S_y \otimes 1_n \rangle)$, the transverse electron observable; (c) $R_{3,3}$, the direct spin–lattice relaxation rate; (d) $R_{4,4}$, the direct spin–spin relaxation rate of the electron. The observable-based formalism adopted here, however, also produces all other single and multispin observables and the associated direct and cross-relaxation terms. For example, in the ^{15}N spin system, there are a total of 16 observables that include one zero-spin operator (which is the constant electron–nuclear identity spin operator, $\langle 1_e \times 1_n \rangle$), six single-spin operators, and nine two-spin operators. The relaxation matrix is the same size as the $\mathcal{L}$ operator matrices and, in this case, is a 16×16 matrix. Similarly, the Liouville-space Hamiltonians are also 16×16 in

dimension. In general these matrices will always be the same size, as suggested by the equations of motion.

Three types of simulations are run: (a) simulation of the observables using eq 2.9 or 2.7; (b) simulations of the correlation functions in eq 2.15 used to determine the numerical R matrix of eq 2.17; (c) simulations of the observables using eq 2.7 or 2.19, and the numerically calculated R matrix .

Separate simulations of the observables using eq 2.7 or 2.9 are used to determine the spin–lattice relaxation rate from the decay of the O_0^1 observable. The number of simulations, N, is sufficiently large that the signal-to-noise ratio in the observables is high enough to extract relaxation rates with high confidence and to produce line shapes with a minimum of filtering. The exact number, N, is set by the SOPHE method in order to uniformly sample the initial orientations of the spin probe. The MC protocol is used to generate N distinct molecular trajectories that provide a set of rotation matrices to reorient the coupling tensors in the Hamiltonians. Each of the simulations is initiated with a driving $\pi/2$ pulse applied to the system, originally at equilibrium at $t = 0$. The amplitude of the pulse, B_0, is as strong as the Zeeman field, 89.2 G, so that significant rotation of the spin system occurs during a mere quarter resonance period (1/4·resonance period, or 1 ns). The functional form of the pulse is $[B_x, B_y, B_z] = B_0[\cos(\omega t + \phi), \sin(\omega t + \phi), 0]$, where ϕ is a random phase used to eliminate spurious correlations in the spectra due to the pulse itself. This driving pulse is incorporated into the L_ω Liouville operator of eq 2.5, and the inhomogeneous solver of eq 2.7 is used to solve the equation of motion while the pulse is on. Once the pulse is turned off, the homogeneous solver of eq 2.9 is used to evolve the spin system. The random underlying molecular process is present while the pulse is on, and while it is off. Thus, there can be pulse-induced relaxation as well as relaxation due to the main static Zeeman field. In practice, relaxation due to the pulse used in these simulations can be ignored due to its short duration. This is the motivation behind the selection of a strong pulse magnitude. Ensemble averaging of the observables is achieved by running N separate simulations, where N was described previously. The return of the O_0^1 to O_{0eq}^1 is averaged over the N runs of the simulation then fit using a nonlinear least-squares Marquardt–Levenberg algorithm for a single ($y = ae^{-rt}$) or double ($y = ae^{-r_1 t} + be^{-r_2 t}$) exponential to the data.[62–64] Ten simulations are run at each diffusion constant to extract an average and standard deviation of the relaxation rates for use in comparing the numerical results to the predictions of BWART in eq B.4. The spin–spin relaxation rates can be determined in a similar manner from the relaxation of transverse magnetization observable, O_1^1, for the spin 1/2 system considered below. In the lab-fixed frame, O_1^1 oscillates at frequencies whose mean is centered at 250 MHz, and whose frequency spread is determined by the width of the coupling tensors (e.g., A or G). In a frame rotating with the observable at the resonance frequency, the rapid 250 MHz oscillations disappear in the O_1^1 observable of the spin 1/2 system and it is possible to fit a single exponential to O_1^1 in a manner similar to that portrayed in Figure 1. For the spin 1/2 system, this is the spin–spin relaxation rate, $R_{2e} \equiv T_{2e}^{-1}$, which can be compared with the $R_{4,4}$ element of the numerical calculation of the Redfield matrix. Simulations of the observables are also used to generate EPR line shapes by using a Zeeman filter described in the literature[44] and included in Appendix D. The NMR absorption spectra are obtained by means of the Fourier
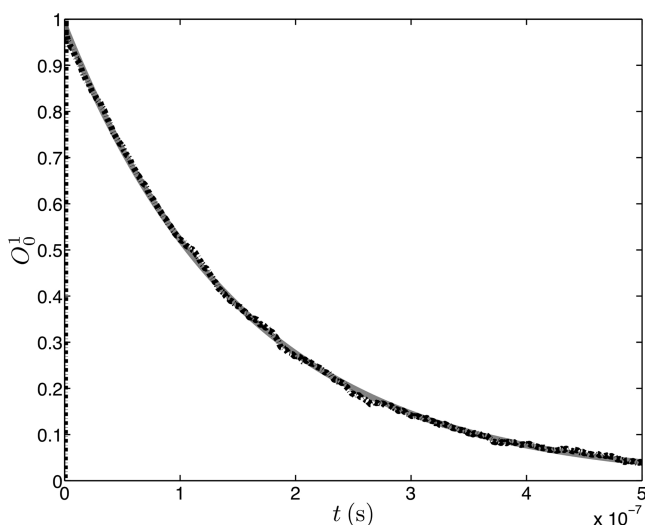
Figure 1. $O_0^1 \equiv \langle S_z \rangle$ plotted as a function of time for a spin 1/2 radical anchored to an isotropically diffusing molecule. The black dotted−dashed line is the simulated observable, O_0^1, and the gray solid line is a single-exponential nonlinear least-squares fit to these data. At $t = 0$, the system is at equilibrium, O_{qeq}^k. A strong pulse is delivered to the spin system initially, and then the magnetization decays to equilibrium via the CSA mechanism with only an 89.2 G Zeeman field present. The driving pulse has a field strength of 89.2 G and is run for 1/4 period, or 1×10^{-9} s. The values of the G tensor in its PAS are given by $G_{xx} = 2.2$, $G_{yy} = 2.6$, and $G_{zz} = 2.9$, and the external Zeeman field strength (89.2 G) is chosen so that the system resonates at 250×10^6 s^{-1}. The underlying molecular trajectory is generated by a Monte Carlo (MC) simulation of a sphere rotationally diffusing with a diffusion constant $D = \omega/6$, where ω is the resonance frequency of the system $(2\pi(250 \times 10^6)$ rad s$^{-1})$. The relaxation rate for this curve is 6.37×10^6 s^{-1}.

transform of the free induction decay following a $\pi/2$ pulse. Rephasing of the imaginary and real parts of the spectra is necessary to account for the zero-time offset due to the time required for the $\pi/2$ pulse.

Simulations of the correlation matrix from eq 2.15 used in calculating R numerically in eq 2.17 require the time step to be shortened in the fast motional regime. This is due to the rather rapid decay in the C function. Calculation of $\overline{L}$ in eq 2.12 is performed in a preliminary simulation averaging over M separate trajectories of length N steps. For the ^{15}N system at the slowest two D values listed above (with $n = \{-20, -15\}$), $\overline{L}$ is obtained separately for each of the M trajectories of length N steps and C functions are calculated from the same trajectories using the separate $\overline{L}$ values. The motivation for this alternative averaging is discussed below.

Once the complete R matrix is calculated numerically, it can be used to simulate the response of the observables in the manner expressed by eqs 2.18 and 2.19. The simulation need only be run once, since all orientation-dependent terms have been preaveraged.

Several test cases for these simulation protocols were selected for comparison with the results of BWART, in particular, the relaxation of the O_0^1 and O_1^1 observables for a single spin 1/2 particle relaxing through the CSA mechanism. The observables of a coupled electron spin 1/2 and nuclear spin 1/2 system are then examined, and the effects of nuclear and electronic CSA and END relaxation mechanisms on the relaxation rates spectra of the electron-only observables are discussed. In these simulations, the underlying motion of the molecular system is that of a spherically symmetric rotating diffusor. To study the

effects of anisotropic motion of a cylindrically symmetric diffusor, an electron spin 1/2 and a nuclear spin 1 multispin system are studied with the spinning rate fixed about a single axis while the spinning around the two orthogonal axes is allowed to vary. In another set of simulations of the spin 1/2−spin 1 system, the Redfield relaxation matrix is determined numerically and used to relax a system. The results are compared to a direct simulation of the corresponding observables. The observables calculated in the simulations are then used to generate line shapes through the use of a Zeeman-filtering technique[44] (see Appendix D). One final set of simulations on a deuterium nucleus coupled to the molecule by a quadrupolar and CSA tensor is performed. The absorption spectrum of this system is calculated by means of the Fourier transform of the appropriate observable.

3.1. Simulations of Spin 1/2 System. The Hamiltonian for a spin coupled to the magnetic components of the light and dc fields of eq 3.1 is now adapted to following the evolution of the spin 1/2 system:

$$H = -\chi_e BGS \tag{3.2}$$

where the values of the CSA tensor in its PAS are given by $G_{xx} = 2.2$, $G_{yy} = 2.6$, and $G_{zz} = 2.9$. The larger-than-physical anisotropy in the CSA tensor was selected for testing purposes to enhance the effects of motion on line shape. Typical values for nitroxyl spin-labels are used later in ^{15}N and ^{14}N simulations.

Simulations were run to determine the spin−lattice relaxation rate from the decay of the O_0^0 observable. In order to avoid aliasing, the time step was chosen to be small compared to the faster of either the diffusion or spin resonance processes. In the observables simulation, 5001 steps with time step $\tau = 1 \times 10^{-10}$ were run for a total time span of 5×10^{-7} s. Ensemble averaging of the observables was achieved by running 947 separate simulations for an isotropically diffusing spin-label. There is no danger of aliasing an rf response as the product of the sampling time and the observer frequency is much smaller than $1/2$.

The return of the O_0^1 to O_{0eq}^1 was fit to a single exponential curve, $y = ae^{-rt}$, to obtain an estimate, r, the spin−lattice relaxation rate. Figure 1 shows excellent agreement between the simulated decay of $\langle S_z \rangle$ and the fit to a single exponential decay.

In Figure 2, the decay rate, measured as shown in Figure 1, is compared with the relaxation rates predicted by BWART for a range of diffusion rates. Relaxation of the magnetization is due to the chemical shift anisotropy (CSA) mechanism alone. Ten simulations were run at each diffusion constant to extract an average and standard deviation of the relaxation rates for use in comparing the numerical results to the predictions of BWART in eq B.4. The results of the best fit to O_0^1 decay curves and the analytical calculations from eq B.4 are shown in Figure 2. Also shown in Figure 2 are the values for $R_{3,3}$ calculated using the method expressed in eq 2.17. The relaxation rates compare well within sampling error.

In Figure 3, typical curves for the $C_{4,4}$ and $C_{3,3}$ elements of the correlation matrix from eq 2.15 used in calculating R numerically in eq 2.17 are shown at three diffusion constants, the lowest of which $(\ln(D) = 17)$ is slow compared to the rotating frame frequency, but intermediate with respect to the range of interest for CW spectra. The $C_{4,4}$ element is the correlation function associated with the direct spin−spin relaxation rate, $R_{4,4}$, that is responsible for the decay of the O_1^1 observable.
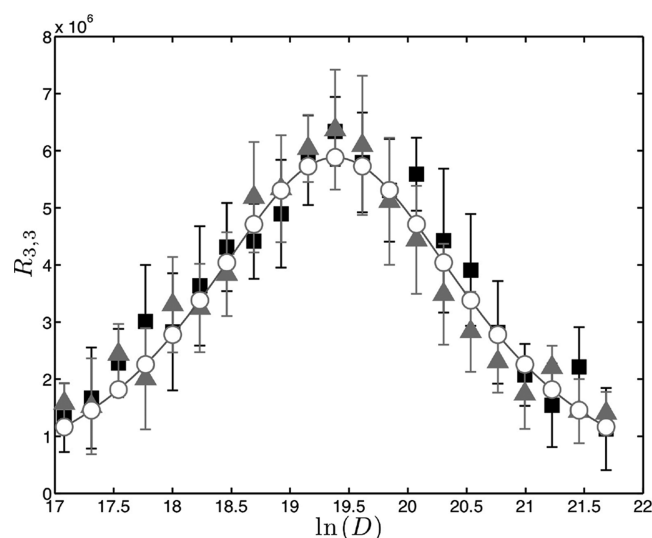
Figure 2. Electron spin–lattice relaxation rate, $R_{3,3}$, plotted versus the natural logarithm of the diffusion constant, $\ln D$, for a spin 1/2 radical anchored to an isotropically diffusing molecule. The spin system is the same used in generating Figure 1. The diffusion constant is chosen to sample slow, intermediate, and fast motional regimes; $D = fD_0$, where $D_0 = \omega/6, f = 10^{n/10}$, and $n = [-10, -9, ..., 0, ..., 9, 10]$. $\omega = 2\pi(250 \times 10^6)$ rad/s is the spectrometer resonance frequency. The maximal relaxation rates occur when $n = 1$, or $\ln D = 19.3831$. The black filled squares represent rates that are calculated from a single-exponential nonlinear least-squares fit to the decay curves of $\Re\{O_0^1\}$. The gray filled triangles represent the (3,3) element of the simulated relaxation matrix, $R_{3,3}$, from eq 2.17. The open circles connected by the solid line are the rates predicted by BWART for R_{1e}, from eqs B.2 and B.4 in Appendix B.
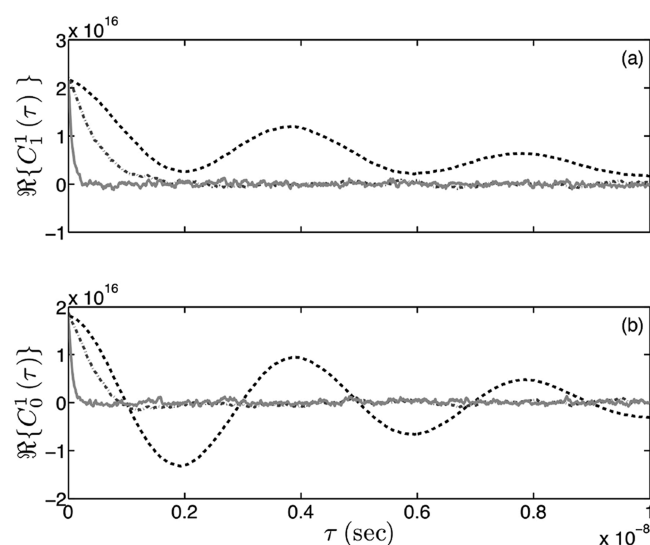
Figure 3. $C_{4,4}$ and $C_{3,3}$ elements of the correlation matrix, C, plotted versus correlation time in (a) and (b), respectively. The spin system is the same as is used in Figure 1. The solid light gray lines are correlation functions for a spin probe undergoing fast rotational diffusion, relative to the spectrometer resonant angular frequency, ω. The diffusion constant in this case is $D = 10(\omega/6)$. The dotted–dashed gray lines are the correlation functions for an intermediate rotational constant of $D = \omega/6$, and the dashed black lines are for a slow rotational constant of $D = \omega/60$.

The spin–spin relaxation rate was obtained from the decay in the transverse magnetization, O_1^1, in the rotating frame, and was

compared with the $R_{4,4}$ element of the numerical calculation of the relaxation matrix. Simulation results shown in Figure 4
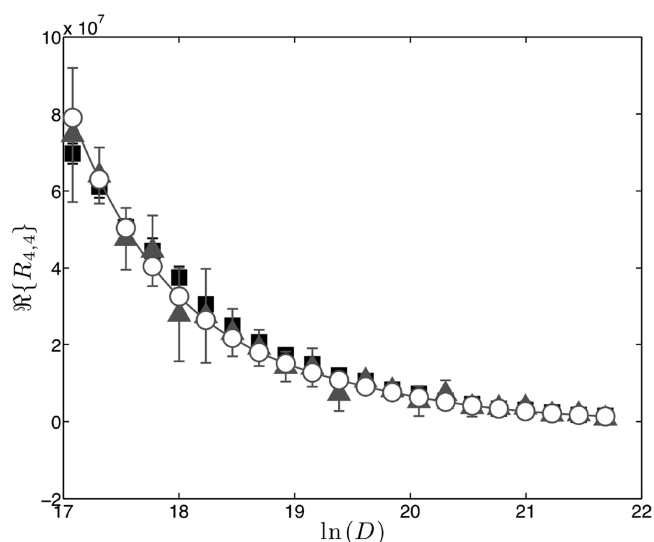
Figure 4. Plot of the real part of the direct spin–spin relaxation rate, $\Re\{R_{4,4}\}$, as a function of the natural logarithm of the diffusion constant obtained from the same simulations as those in Figure 2. The squares are calculated by fitting a single exponential to the decay of the real part of O_1^1 in the rotating frame, which is calculated from O_1^1 as $e^{-i\omega t}O_1^1$. The gray filled triangles are the values for $R_{4,4}$ determined numerically from the integral of $C_{4,4}$ (see eq 2.17). Examples of $C_{4,4}$ are shown in Figure 3. The open circles connected by the solid line are the rates predicted by BWART for R_{2e}, from eq B.6 in Appendix B.

indicate that the apparent relaxation rate continues to increase as the motion slows, the origin of which can be seen in the offset in the oscillations observed in the $C_{4,4}$ element plotted in Figure 3. In contrast, the oscillations of $C_{3,3}$ occur about zero and therefore cancel, leading to the observed decrease in the direct spin–lattice relaxation rate, $R_{3,3}$, as molecular motion slows. The oscillations that appear for $D < \omega/6$ in parts a and b of Figure 3 are of the same frequency. This oscillation in the slower motion regime is predicted by a theory of relaxation presented in the literature[41] and shows why BWART works only in the fast motion limit. Simulations at diffusion constants below those shown in Figure 4 were performed, and the CW spectra obtained directly from the S_+ observable correctly approaches the powder-pattern slow motion limit. This direct simulation result is in agreement with expectations based on CW spectra and relaxation rates obtained from spin–echo methods; there should should be an upper limit on the spin–spin relaxation rate. However, the analytic forms for spin–spin relaxation from BWART diverge because the spectral density that appears in those expressions increase with the diffusion correlation time, τ. The numerical method for calculating $R_{4,4}$ from eq 2.17 also diverges, as is expected, since the method is a numerical implementation of BWART. Extracting the spin–spin relaxation in this slow motion limit, at diffusion constants below those shown in Figure 4, by fitting the decay in the transverse magnetization, O_1^1, in the rotating frame, fails due to the presence of complex oscillations in the exponential decay that originate in broadening due to the CSA. The ability to incorporate pulse experiments into the simulation formalism provided in this work should allow for direct comparison with spin–echo experiments and lead to a direct test of the simulation of observables and experiment.

3.2. Simulations of the Nitroxyl ^{15}N Spin System.
Simulations of a nitroxyl ^{15}N spin system (spin 1/2 electron coupled to a spin $1/2 \,^{15}$N nucleus) are run to examine the effects of direct and cross-relaxation on the decay of the spin−lattice relaxation and to compare with predictions of BWART. The Hamiltonian governing the evolution of the spin system is

$$H = -\gamma_e BG_e S + \gamma_n BG_n I + IAS \qquad (3.3)$$

The system is run at 250 MHz, with $G_{exx} = 2.002$, $G_{eyy} = 2.006$, and $G_{ezz} = 2.009$, and $G_{nxx} = G_{nyy} = G_{nzz} = 0.0137$. The END tensor, A, has principal axis components given by $A_{xx} = 8.8371$, $A_{yy} = 8.2760$, and $A_{zz} = 44.8870$ G.

Spin−lattice relaxation rates are calculated from the decay of $O_{0,0}^{1,0}$ for an isotropically diffusing spin probe. In the observables simulation, 10^4 steps with time step $\tau = 1 \times 10^{-10}$ were run for a total time span of 1×10^{-6} s. Ensemble averaging of the observables was achieved by running 947 separate simulations with the initial orientation of the molecular frame determined by SOPHE.

In Figure 5, the $R_{3,3}$ relaxation rates are plotted over a range of diffusion constants. The electron spin−lattice relaxation rate
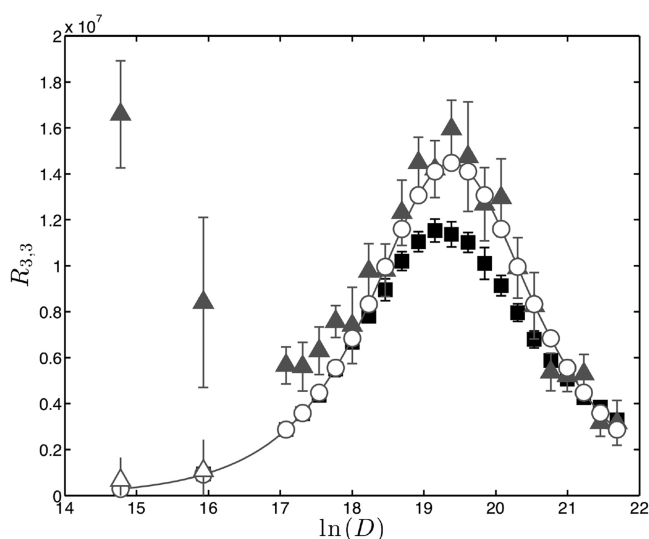
Figure 5. Electron spin−lattice relaxation rate for an ^{15}N-nitroxyl radical (coupled spin 1/2 electron−spin 1/2 ^{15}N nucleus multispin system) anchored to an isotropically diffusing molecule. The rate is computed by three methods. The gray filled triangles represent the (3,3) element of the simulated relaxation matrix, $R_{3,3}$, from eq 2.17 using an average Liouvillian ($\bar{L}$ of eq 2.12) preaveraged over 947 trajectories, each of which is 10^5 moves long ($M = 947$ and $N = 10^5$ in eq 2.12). The open triangles are also calculated using eq 2.17, but use an average Liouvillian ($\bar{L}$ of eq 2.12) recalculated separately for each trajectory ($M = 1$ and $N = 10^4$ in eq 2.12). The open circles connected by the solid line are the rates predicted by BWART for R_{1e}, from eqs B.2 and B.4 in Appendix B. The filled black squares are the rates calculated directly from the decay of the $O_{0,0}^{1,0}$ observable through a single exponential nonlinear least-squares fit to the data. The relaxation is due to the CSA and END mechanisms of the electron for this system. The values of the electron G tensor in its PAS are given by $G_{xx} = 2.002$, $G_{yy} = 2.006$, and $G_{zz} = 2.009$, and the external Zeeman field strength is chosen so that the system resonates at 250×10^6 s^{-1}. The values of the END A tensor are given by $A_{xx} = 8.8371$, $A_{yy} = 8.2760$, and $A_{zz} = 44.8870$ (in gauss). The maximal relaxation rate from BWART occurs for $D = \omega/6$, whereas the simulated maximum value occurs at $D = 0.7943(\omega/6)$.

is less than what is predicted by BWART (see Appendix B), and the maximum rate is shifted to a lower diffusion constant than what is predicted. The numerically determined rate calculated using eqs 2.18 and 2.19 diverges from BWART predictions for diffusion constants below $\ln(D) = 18.5$. As discussed in section 3.1, it is expected that $R_{4,4}$ rates should fail at the lower diffusion constants due to a divergence in the correlation functions. The deviations in $R_{3,3}$ rates from those predicted by BWART and from those obtained by direct fitting of $O_{0,0}^{1,0}$ are not expected, since the rates from BWART do not diverge as the diffusion coefficient becomes small, and serves as the basis for the development of eq 2.17.

To determine whether the method used to calculate the average Liouvillian in eq 2.12 was the source of the discrepancy at $\ln(D) \approx 14.8$ and $\ln(D) \approx 15.9$ (Figure 5), calculations were performed in which $\bar{L}$ was determined for each trajectory when calculating the correlation function $C(t)$. In Figure 5, the two values of $R_{3,3}$ are plotted along with the other data and now agree with BWART predictions and the values extracted from fitting the direct simulation.

3.3. Simulations of the Nitroxyl ^{14}N Spin System.
Simulations of a nitroxyl ^{14}N spin system (spin 1/2 electron coupled to a spin $1\,^{14}$N nucleus) were run to compare isotropic and anisotropic rotational diffusion. In these simulations, $G_{xx} = 2.002$, $G_{yy} = 2.006$, and $G_{zz} = 2.009$. The END tensor, A, has principal axis components given by $A_{xx} = 6.3$, $A_{yy} = 5.9$, and $A_{zz} = 32.0$ G. The Hamiltonian is the same used in eq 3.3. In the observables simulation, 10^4 steps with time step $\tau = 1 \times 10^{-10}$ were run for a total time span of 1×10^{-6} s. Ensemble averaging of the observables was achieved by running 947 separate simulations with the initial orientation of the molecular frame determined by SOPHE.

In Figure 6, the spin−lattice relaxation rate determined from the trajectories is less than predicted by BWART, and the maximum rate is slightly shifted to a higher diffusion constant. The numerically determined rate calculated using eqs 2.18 and 2.19 diverges from BWART predictions for diffusion constants below $\ln(D) = 19$. It is anticipated that proper averaging of $\bar{L}$ in the calculation of the C functions will resolve these differences, as was the case in the ^{15}N-nitroxyl radical simulations discussed above.
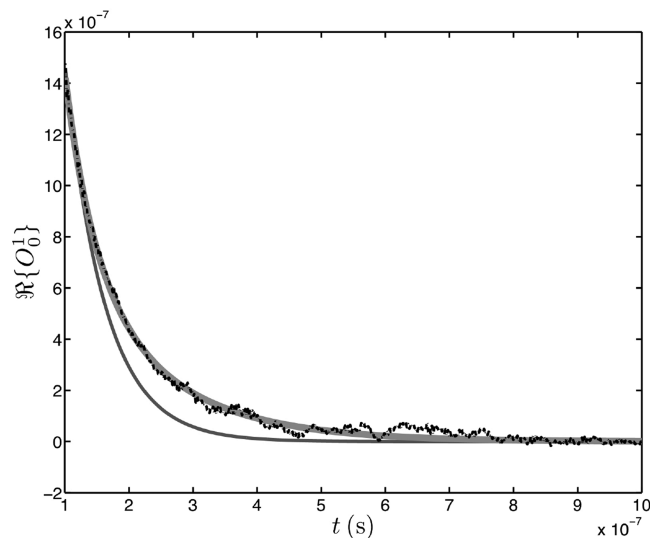
In Figure 7, single and double exponential fits to $O_{0,0}^{1,0}$ for an ^{14}N-nitroxyl radical anchored to an isotropically diffusing molecule are contrasted. The error between the numerically simulated $O_{0,0}^{1,0}$ observable using eq 2.7 and the double exponential fit is noticeably smaller than that between the simulated $O_{0,0}^{1,0}$ and a single exponential fit.

Based on the improved fit of a multiexponential fit to the data, a double exponential is fit to all the decays of $O_{0,0}^{1,0}$ for an ^{14}N-nitroxyl radical across the range of diffusion constants. In Figure 8, the results of this fitting procedure are plotted along with the previous single exponential fits, for comparison. Across the range of diffusion constants tested, the two rates predicted by the multiexponential fit bracket the single rate predicted by BWART.

In Figure 9, the effects of anisotropic diffusion are apparent in the slower motional regime. The rapid rotation about the y-axis prevents the system from relaxing in the slow motion limit even though the diffusion about the x- and z-axes is considerably slower. The spin−lattice relaxation rate is less than what is predicted from BWART; these data may be also be analyzed by a biexponential decay curve to explain the discrepancy. The numerically determined rate calculated using
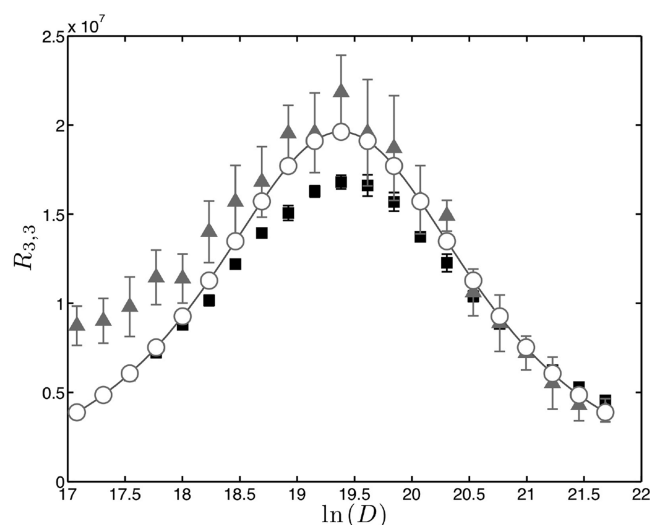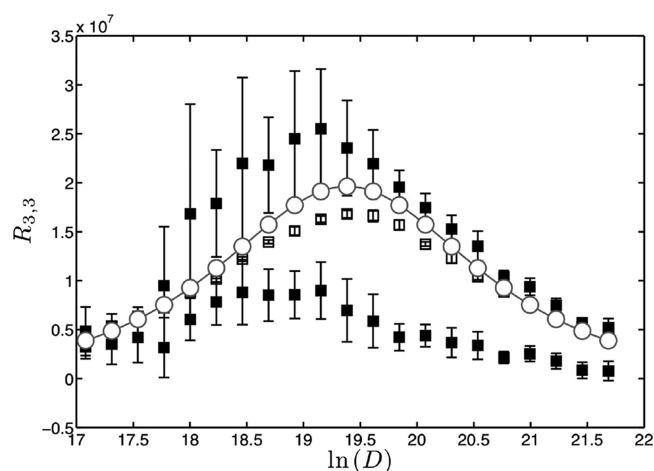
Figure 6. Electron spin−lattice relaxation rate for an ^{14}N-nitroxyl radical (coupled spin 1/2 electron−spin 1 ^{14}N nucleus multispin system) anchored to an isotropically diffusing molecule. The rate is computed by three methods: the gray filled triangles represent the (3,3) element of the simulated relaxation matrix, $R_{3,3}$, from eq 2.17. The open circles connected by the solid line are the rates predicted by BWART for R_{1e}, from eqs B.2 and B.4 in Appendix B. The filled black squares are the rates calculated directly from the decay of the $O_{0,0}^{1,0}$ observable through a single exponential nonlinear least-squares fit to the data. The relaxation is due to the CSA and END mechanisms of the electron for this system. The values of the electron G tensor in its PAS are given by $G_{xx} = 2.002$, $G_{yy} = 2.006$, and $G_{zz} = 2.009$, and the external Zeeman field strength is chosen so that the system resonates at 250×10^{6} s^{-1}. The values of the END A tensor are given by $A_{xx} = 6.3$, $A_{yy} = 5.9$, and $A_{zz} = 32.0$ (in gauss). The maximal relaxation rate from BWART occurs for $D = \omega/6$, whereas the simulated maximum value occurs at a slightly higher value of D.


Figure 7. Comparison of single (thin dark gray line) and double (thick light gray line) exponential fits to $O_{0,0}^{1,0} \equiv O_{0}^{1}$ (dotted−dashed black line) for an ^{14}N-nitroxyl radical anchored to an isotropically diffusing molecule. The diffusion constant is $D = \omega/6$, and the parameters describing the magnetic system are those described in Figure 6.

eqs 2.18 and 2.19 compares well with the BWART predictions over the full range of diffusion constants considered here. The agreement between the predictions of eqs 2.18 and 2.19 for the

Figure 8. Comparison of single and double exponential fits to the $O_{0,0}^{1,0}$ observable for an ^{14}N-nitroxyl radical anchored to an isotropically diffusing molecule. The filled squares are the two rates extracted from the fits at each diffusion constant. The rates obtained from a single exponential fit to $O_{0,0}^{1,0}$ (open squares) and the rates predicted by BWART (open circles) are shown for comparison. The simulation data used in this figure are the same that appear in Figure 6.
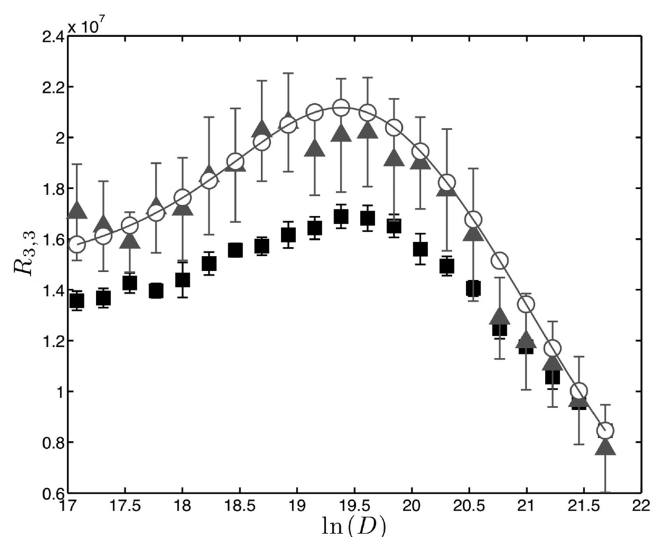

Figure 9. Plot of electron spin−lattice relaxation rate for an ^{14}N-nitroxide radical anchored to an anisotropically diffusing molecule. The rate is computed by three methods: the gray filled triangles represent the (3,3) element of the simulated relaxation matrix, $R_{3,3}$, from eq 2.17. The open circles connected by the solid line are the rates predicted by BWART for R_{1e}, from eqs B.2 and B.4 in Appendix B. The black filled squares are the rates calculated directly from the decay of the $O_{0,0}^{1,0}$ observable through a single exponential nonlinear least-squares fit to the data. The parameters describing the magnetic system are those described in Figure 6. The diffusion constants for a cylindrically symmetric molecule oriented along the x-axis are $D_{yy} = D_{zz} = fD_{xx}$, where $D_{xx} = \omega/6$ and $f = 10^{n/10}$ with $n = [-10, -9, ..., 0, ..., 9, 10]$.

direct spin−lattice ($R_{3,3}$) relaxation rate over the motional regime for which these mechanisms give substantial spin−lattice relaxation rates is predicted by BWART, as is discussed in the literature.[11,15,43] Estimates for $R_{3,3}$ from eqs 2.18 and 2.19 or those of BWART do *not* diverge from the value drawn from the direct method, though a divergence for the direct spin−spin

relaxation rate, $R_{4,4}$, is anticipated for diffusion constants below those used in this paper.[11,15,43]

3.4. Simulation Using the Numerical R Matrix. In these simulations, the decay of the $O_{0,0}^{1,0}$ observable ($\langle S_z \rangle$ of the electron) in a nitroxyl ^{15}N spin system (spin 1/2 electron coupled to a spin 1/2 ^{15}N nucleus) is compared to that obtained using a numerically calculated relaxation matrix (R) according to eqs 2.18 and 2.19. The average Hamiltonian in eq 2.12 is calculated with $M = 4000$ trajectories, each of which is run for 1 μs sampled at 5×10^{-10} s intervals. The values of G and A used are the same as those used in the trajectory simulations of section 3.2. The R matrix is averaged over 10^4 trajectories. The diffusion constant for these simulations is $D = \omega/6$, which corresponds to a motional regime in which the inverse of the characteristic molecular diffusion time scale and Larmor frequency are similar.

The results of these simulations are shown in Figure 10, in which the trajectory-based $O_{0,0}^{1,0}$ observable is compared with the
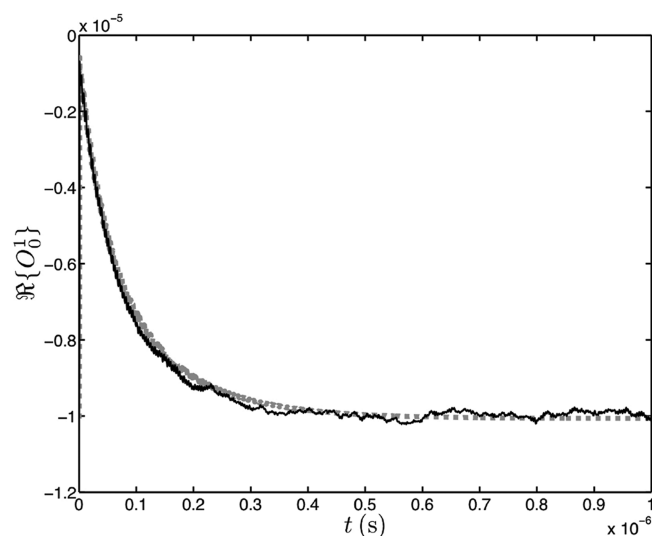

Figure 10. Decay of the $O_{0,0}^{1,0} \equiv O_0^1$ observable of an ^{15}N-nitroxyl radical anchored to an isotropically diffusing molecule. The solid black line is the decay curve calculated by running a trajectory according to eqs 2.18 and 2.19 with the numerically calculated R matrix of eq 2.17. The dashed gray line is the $O_{0,0}^{1,0}$ observable obtained directly from trajectory simulations. The diffusion constant for this simulation is $D = \omega/6$. where $\omega = 2\pi(250 \times 10^6)$ and the magnetic parameters are those used in Figure 5. (See Figure 5 for rates determined at other diffusion constants.) The pulse that initiates the simulation is the same as that described in Figure 1 and is included in this figure to demonstrate the direct inclusion of a time-dependent field in the equations of motion that drives the system away from equilibrium.

same observable computed using eqs 2.18 and 2.19. Within the accuracy of the calculations, agreement is achieved between the two simulations. The pulse that initiates the simulation by driving the spin system away from equilibrium is shown in Figure 10 to demonstrate the direct inclusion of a time-dependent field in the equations of motion. The pulse occurs during the first nanosecond, so its effect on $O_{0,0}^{1,0}$ is short compared to the relaxation rate, as is evident in Figure 10.

3.5. EPR and NMR Spectra. EPR line shapes are shown in Figures 11 and 12 for an electron spin coupled to either a spin 1/2 (^{15}N) or a spin 1 (^{14}N) nucleus calculated from the time-domain simulations of the observables. In these spectra, the first harmonic absorption, A_1, in the low modulation limit is plotted.
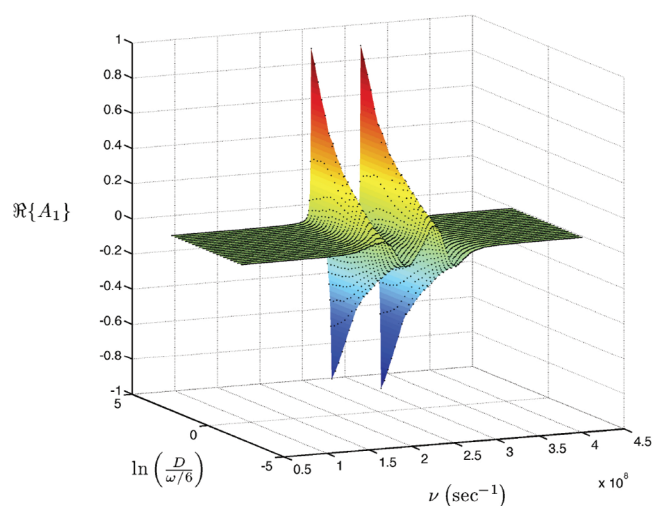

Figure 11. Plot of $\Re\{A_1\}$, the real part of the first harmonic of the Zeeman-filtered spectrum of $O_{0,0}^{1,0}$, for an ^{15}N-nitroxide radical anchored to an isotropically diffusing molecule. $\Re\{A_1\}$ is plotted as a function of frequency and the natural logarithm of the diffusion coefficient normalized by $\omega/6$, where $\omega = 2\pi(250 \times 10^6)$ rad/s is the spectrometer resonance frequency. Diffusion and magnetic constants in the simulation are the same as those in Figure 5. The Zeeman filter is set at 0.05ω or 8.9208 G. The phase of the first-harmonic signal is rotated by an angle of 10° to adjust for the effects of the pulse that initiates the simulation.
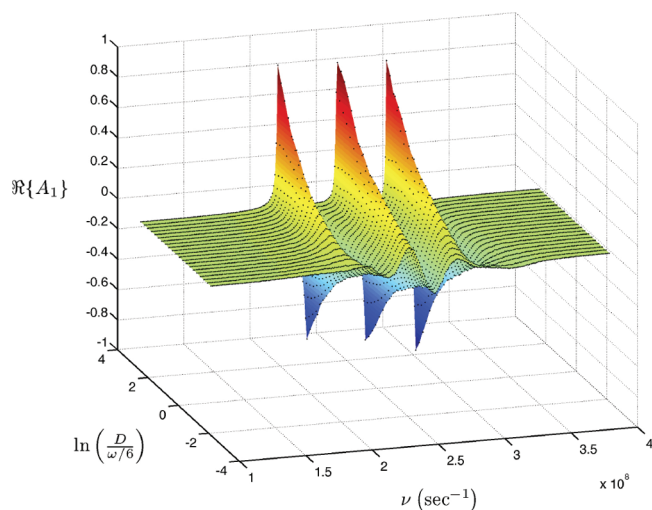
Figure 12. Plot of $\Re\{A_1\}$, the real part of the first harmonic of the Zeeman-filtered spectrum of $O_{0,0}^{1,0}$, for an ^{14}N-nitroxide radical anchored to an isotropically diffusing molecule. $\Re\{A_1\}$ is plotted as a function of frequency and the natural logarithm of the diffusion coefficient normalized by $\omega/6$, where $\omega = 2\pi \times 250 \times 10^6$ rad/s is the spectrometer resonance frequency. Diffusion and magnetic constants in the simulation are the same as those in Figure 6. The Zeeman filter is set at 0.045ω or 8.0287 G. The phase of the first-harmonic signal is rotated by an angle of 5° to adjust for the effects of the pulse that initiates the simulation.

A detailed discussion of the modulation filter can be found in the literature,[44] and the equation used for calculating the nth harmonic is included in Appendix D. In Figure 13, the spectrum of the Fourier transform of the $\langle I_+ \rangle$ observable of spin 1 nucleus in a NMR quadrupolar simulation is shown. The effects of homogeneous broadening due to mechanisms not
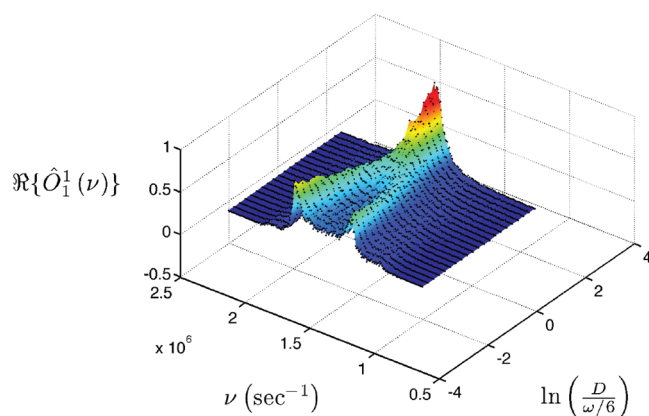
Figure 13. Absorption spectrum of a nucleus interacting with the bath via quadrupolar relaxation with $q = 2\pi(170 \times 10^3)$. Here, the real part of the Fourier transform of O_1^1, or $\Re\{\tilde{O}_1^1\}$, is plotted as a function of frequency and the natural logarithm of the diffusion constant normalized by $\omega/6$, where $\omega = 2\pi(1.7 \times 10^6)$ rad/s is the spectrometer resonance frequency. The phase of the Fourier-transformed signal is rotated by a phase angle of $-15°$ to adjust for the effects of the pulse that initiates the simulation.

included in the simulation can be added to the results by filtering the data with a time-dependent exponential decay function. Inhomogeneous effects omitted from the simulation can be included through the use of a Gaussian filter.[65] A unitless quadrupolar Hamiltonian coupling tensor, Q, is used in the simulation and has principal axis components given by $Q_{xx} = 1$, $Q_{yy} = 1$, and $Q_{zz} = -2$, and a magnitude of $q = 2\pi(170 \times 10^3)$ rad/sec. The Zeeman field is set so that the system is resonant at 1.7 MHz. The field is reduced here for computational efficiency without loss of generality since the Fourier transform spectrum of $\langle I_+ \rangle$ is only minimally affected by the $R_{3,3}$ rates. The line widths observed in the spectra are generated directly from the nonstationary terms in the deuterium quadrupolar relaxation tensor with no additional broadening.

4. DISCUSSION AND CONCLUSION

Equation 2.1 serves as the foundation for the method presented in this article. This equation indicates explicitly that the Hamiltonian of the driving field must act on the entire density matrix, as confirmed by simulations. In contrast, the remaining (fluctuating) Hamiltonians of the system operate on the difference of the full and equilibrium density matrices, so the stochastic fluctuations drive the density matrix to its equilibrium value. By arranging simulations according to the rules prescribed by eq 2.1, it is possible to both drive the system at equilibrium to its perturbed state during a magnetic pulse and relax the system to a nonzero equilibrium state following excitation. Simulations showed that allowing the full Hamiltonian to operate on either the full or difference density matrices alone was not sufficient to mimic the results of experiments.

An interesting point of discussion arises in relation to the random component of the driving field Hamiltonian, H_ω, of eq 2.4, and its relaxation effects. The coupling tensor, G, in H_ω fluctuates as its PAS is rotated by the underlying molecular motions. A more detailed analysis would incorporate these fluctuations into the simulation, thereby allowing for an investigation of their effects on the overall relaxation of the

system. This would be accomplished by isolating the secular and pseudosecular portions of H_ω from the nonsecular parts. The additional fluctuations in H_ω might be added to the Hamiltonian H acting on the difference density matrix to factor in this additional relaxation mechanism. This procedure could be important in simulating CW spectra where the driving field is left on throughout the simulation. In the simulations performed in this work, the duration of the pulse was short so that the effect on relaxation was minimal.

The relaxation effects of spin rotation[15,42,66] (SR) were also not considered in the simulations of the observables; the time scale for spin rotation is several orders of magnitude faster than that of the diffusion regimes considered, which makes direct sampling of both motions at the same time challenging. A possible alternative to direct sampling (in time) is to calculate the relaxation matrix from simple analytical BWART expressions for spin-rotation relaxation and include that in the relaxation matrix, R, in the Liouville space equation of motion. This would permit one to incorporate the effects of SR from analytic theory into the trajectory method simulations. Initial calculations (not shown) demonstrate that the methodology is general enough to accurately capture such relaxation effects. Potentially, additional relaxation mechanisms not explicitly included in the fluctuating Hamiltonian may be treated in a similar manner. The numerical method for determining the relaxation matrix is easily implemented and serves as a means to simulate dynamical systems with simultaneous distinct slow and fast motions. The averaged Liouvilian, $\bar{L}$, obtained in eq 2.12 and the remaining fluctuations, L_f, obtained in eq 2.13, arise spontaneously from the underlying dynamics of the molecular system and do not require the approximations necessary when making a similar partitioning in BWART. Oganesyan[31] has similarly made use of a stochastically averaged Liouvillian in propagating the density matrix of the spin systems studied in that work. In our studies, we have found that $\bar{L}$ must be obtained separately for each calculation of the C function used in calculating R. The alternate method of pre-averaging over M trajectories to obtain $\bar{L}$ is at the root of the discrepancy between the $R_{3,3}$ values obtained via eq 2.17 and BWART predictions and direct fitting of the simulated observable, S_z.

The spin−lattice relaxation rates were simulated across the motional regime where these operators contribute to the spin−lattice relaxation. The range over which these mechanisms provide relaxation can be understood in terms of the analytic theory, which shows that the spectral density functions for spin−lattice relaxation for these mechanisms centers around the spectrometer frequency. The trajectory method produces results in agreement with known solutions of the BWART in the case of a single spin 1/2 system with a CSA relaxation mechanism, which is important for both the BWART and the numerically intensive trajectory-based method. However, when the CSA and END mechanisms are present in the multispin systems, the rates deviate from those calculated by the BWART, especially when the spectrometer frequency is competitive with the diffusional correlation time of the molecular system. The observed relaxation of the $\langle S_z \rangle$ magnetization is best described by a multiexponential rather than single exponential function, as is suggested by BWART. When analyzed with a sum of two exponentials, the two rates extracted bound the BWART predicted rate from above and below. A more detailed treatment of how to use BWART that mixes direct and cross-relaxation rates and causes $\langle S_z \rangle$ to be

multiexponential can be found in Robinson et al.[11] and Abragam[3] and serves as the motivation for a theoretical foundation on which to base fitting of data to a biexponential. Thus, analyzing recovery rate data should be done with care, especially when trying to differentiate the effects of complex motions from the effects of cross-relaxation mechanisms that lead to multiexponential decay functions for spin probes undergoing rigid-body isotropic rotation. The agreement between the extended BWART found in Robinson et al.[11] and Abragam[3] and the values obtained by fitting the decay in S_z to a multiexponential function lends confidence to the data-fitting approach of sections 3.1, 3.2, and 3.3. The origin for the discrepancy between the values of the spin−lattice relaxation rates calculated using the methods in section 2.2 is that the average Hamiltonian used in the method is calculated from an ensemble of trajectories, rather than an average over just the trajectory used to generate the fluctuations. The latter averaging technique improves the agreement between the various estimates of the spin−lattice relaxation, as is shown in Figure 5.

Over the range of diffusion constants tested, BWART and simulated spin−spin relaxation rates agree. However, BWART produces an expression for the transverse relaxation rate that increases without bound as molecular motion slows——a prediction that contradicts experimental observations (e.g., CW spectra, spin−echo results). In the slow motion limit, the line widths vanish as the molecular motion decreases, and the direct numerical simulations of observables using eqs 2.7 and 2.9 correctly generate a free-induction decay (FID) of S_+ with a small R_2 rate. Since BWART is expected to produce erroneous results in the slow motion limit, and eq 2.17 is a numerical implementation of the BWART methodology, it also produces divergent predictions for the spin−spin relaxation rate. Analysis through exponential fitting of the decay of the S_+ observable obtained from direct simulation is not possible in the slow motion limit due to the appearance of oscillations in the time-domain FID that make such a fitting fail. The comparison of CW spectra with known solutions or experiment is the alternative, as has been pursued in numerous other studies.[26,28,29,31,33] The ability to simulate spin−echo experiments using eqs 2.7 and 2.9 offers another avenue for direct comparison with spin−echo experiments, and the potential to extract a spin−spin relaxation rate directly from simulation.

In contrast, BWART predictions of R_1 do correctly predict rates in the slow motion limit,[11,15,43] and agree with simulation results as discussed above. The discrepancy between the values obtained using eq 2.17 and either BWART or direct simulation of the observables is not expected, since the method is a numerical implemenation of BWART, and that theory does not fail in its predictions for R_1.

The techniques presented in this work allow for the comparison of the effects of BWART with a direct method to simulate rates and line shapes simultaneously. Because all components of the CSA, END, and DQR Hamiltonians are used, the method performs well and offers two approaches to calculate the spin−lattice relaxation rate for comparison with BWART. The direct method of fitting the decay of the $\langle S_z \rangle$ observable to extract the spin−lattice relaxation rate shows that this approach faithfully converts molecular trajectories into spectra.

The numerical procedure to calculate the entire R matrix from trajectories produces spin−spin relaxation rates equal to those obtained with the direct method for all diffusion regimes in the case of a single spin 1/2 particle, and rates that are comparable within numerical accuracy for diffusion rates for the electron spin coupled to either a spin 1/2 (^{15}N) or a spin 1 (^{14}N) nucleus. The $\langle S_z \rangle$ observable generated using the calculated R matrix faithfully reproduces the evolution of S_z obtained using the direct method. By calculating R, one obtains an estimate of all relaxation mechanisms that contribute to the evolution of the spin system, and may directly simulate all MR observables, not just $\langle S_z \rangle$ as is done here for demonstration purposes. However, since the calculation of R is based on the numerical implementation of BWART and that theory is known to fail in the slow motion limit, this method cannot be used to simulate in this regime.

To demonstrate the wide applicability of simulation methodology presented in this work, ^2H NMR DQR spectra are calculated. No modification of the method is required to simulate pulsed NMR measurements; eqs 2.6 and 2.7 indicate how to simulate such experiments.

■ APPENDIX A: DERIVATION OF THE INHOMOGENEOUS SOLVER

In this appendix, a derivation of eqs 2.7 and 2.9 in section 2.1 is provided. The solutions are repeated here for convenience. The homogeneous solution is

$$\Delta O(t_0 + \tau) = e^{-i\tau L(t_0)} \Delta O(t_0) \tag{A.1}$$

while the inhomogeneous solution is

$$O(t_0 + \tau) = e^{-i\tau(L(t_0) + L_\omega(t_0))} O(t_0)$$
$$- \tau/2(e^{-ia\tau L(t_0)} + e^{-ib\tau L(t_0)}) O_{in}(t_0) \tag{A.2}$$

where $a + b = 1$, $a^2 + b^2 = 2/3$ and $O_{in}(t_0) = iL(t_0)O_{eq}$. The solution given in eq A.1 to the homogeneous differential equation is obtained directly from the formal matrix exponential solution by using the assumption that for small time steps, τ, the fluctuating Hamiltonian is nearly constant. This implies that the sampling rate must be at least an order of magnitude faster than the time scale of the dynamical motion of the molecular system.

In the case of the inhomogeneous problem

$$\frac{dO(t)}{dt} = -iL_T(t)\, O(t) + O_{in}(t) \tag{A.3}$$

where $L_T(t) = L(t) + L_\omega(t)$ and $O_{in}(t) = iL(t)O_{eq}$, the derivation of the expression in eq A.2 begins by seeking an integrating factor, $c(t)$ for eq A.3. Multiplying eq A.3 by the unknown $c(t)$, one finds that

$$c\frac{dO}{dt} + icL_T O = cO_{in} \tag{A.4}$$

Adding and subtracting $(dc/dt)O$ from the left-hand side of eq A.4, one obtains

$$c\frac{dO}{dt} + \frac{dc}{dt}O - \frac{dc}{dt}O + icL_T O = cO_{in} \tag{A.5}$$

A solution is possible if $dc/dt - icL_T = 0$, which leads to the integrating factor

$$c(t) = e^{i\int_{t'=t_0}^{t'=t} L_T(t')\,dt'} \tag{A.6}$$

The formal solution to eq A.3 using the integrating factor in eq A.6 is

$$O(t_0 + \tau) = e^{-i\int_{t'=t_0}^{t'=t_0+\tau} L_T(t')\,dt'}\left[\int_{t''=t_0}^{t''=t_0+\tau} e^{i\int_{t'=t_0}^{t'=t''} L(t')\,dt'} O_{in}(t'')\,dt''\right]$$

$$+ e^{-i\int_{t'=t_0}^{t'=t_0+\tau} L_T(t')\,dt'} O(t_0) \tag{A.7}$$

For integration time interval, τ, small compared to the rate of change in $L(t)$

$$c(\tau) = e^{i\int_{t'=t_0}^{t'=t_0+\tau} L_T(t')\,dt'}$$

$$\approx e^{iL_T(t_0)\tau} \tag{A.8}$$

so that eq A.7 becomes

$$O(t) = e^{-i\tau L_T(t_0)}\left[\int_{t''=t_0}^{t''=t_0+\tau} e^{i(t''-t_0)L_T(t_0)}\,dt''\right] O_{in}(t_0)$$

$$+ e^{-i\tau L_T(t_0)} O(t_0) \tag{A.9}$$

The integral in brackets is equal to $-i(e^{i\tau L_T(t_0)} - 1)L^{-1}$. Since L_T is Hermitian, there exists a similarity transformation such that

$$\Lambda = T^{-1}L_T T \tag{A.10}$$

For T and Λ it is also true that $L_T^{-1} = T\Lambda^{-1}T^{-1}$ and $e^{\tau T\Lambda T^{-1}} = Te^{\tau\Lambda}T^{-1}$ so that eq A.9 can be rewritten as

$$O(t_0 + \tau) = \tau T X(\chi(t_0))T^{-1}O_{in} + Te^{-i\chi(t_0)}T^{-1}O(t_0) \tag{A.11}$$

where

$$X(\chi(t_0)) = -\frac{1 - e^{-i\chi(t_0)}}{-i\chi(t_0)} \tag{A.12}$$

and

$$\chi(t_0) = \tau\Lambda(t_0) \tag{A.13}$$

For vanishing eigenvalues, $\chi_{ii} = 0$ and $\lim_{\chi_{ii}\to 0} X_{ii} = 1$, whereas off-diagonals are 0 by virtue of the symmetry of L. Thus, a solution exists in such cases, but care must be taken numerically to avoid instability at these points. In practice, this can be accomplished by setting $X_{ii} = 1$ whenever $|\chi_{ii}| \leq 1 \times 10^{-6}$. However, checking every eigenvalue against this condition is computationally inefficient and introduces error. Instead, we Taylor expand X in χ. This is always possible for any Λ since we are free to choose τ as small as required to ensure that $\chi \ll 1$. The expansion is

$$X = -\sum_{n=0}^{\infty} \frac{(-i\chi)^n}{(n+1)!} \tag{A.14}$$

In practice, use of a truncated Taylor series to second order in eq A.14 is undesirable since such an approximation would require short time steps in order to maintain accuracy. It would be advantageous to find an alternate expansion of X that maintained accuracy to higher order, but did not require further evaluations of the matrix exponential (the most time-consuming step in the calculations). To achieve this goal, we express X as a sum of two exponentials:

$$X = -\frac{1}{2}(e^{-ia\chi} + e^{-ib\chi}) \tag{A.15}$$

Equation A.15 can be equated to eq A.14 to determine the values of a and b that provide an approximation of X. After expanding both exponentials in eq A.15, collecting coefficients of like powers of χ, and equating them to the Taylor

coefficients in eq A.14, one finds that to third order in χ a and b satisfy

$$a + b = 1 \tag{A.16}$$

$$a^2 + b^2 = \frac{2}{3} \tag{A.17}$$

The third order coefficients in the expansions are automatically equal if the first and second order coefficients are used to solve for a and b so that the approximation of X is exact to third order. Higher order terms are very nearly exact; since $c = ((n+1)/2)(a^n + b^n)$ needs to be 1 for the nth term to be exact, and since, for $n = 4, 5, 6, 7$, $c = 0.97, 0.92, 0.84, 0.76$, respectively, then these higher order terms are also rather close approximations. Using these results, the approximate solution to the inhomogeneous ordinary differential eq A.3 is

$$O(t_0 + \tau) = -\frac{\tau}{2}T(e^{-ia\tau\Lambda(t_0)} + e^{-ib\tau\Lambda(t_0)})T^{-1}O_{in}(t_0)$$

$$+ T(e^{-i\tau\Lambda(t_0)})T^{-1}O(t_0) \tag{A.18}$$

which is the expression given for the approximate solution in eq A.2 after the T similarity transformation is reintroduced into the exponentials.

■ APPENDIX B: EXPRESSIONS FOR $R_{3,3}$ AND $R_{4,4}$ FROM BWART

According to the BWART of relaxation, the total relaxation rate due to the combined effects of the chemical shift anisotropy (CSA) and electron−nuclear dipolar (END) mechanisms is $R_{3,3} = R_{3,3}^{END} + R_{3,3}^{CSA}$ where the individual rates are given as follows. The END spin−lattice relaxation rate for a cylindrically symmetric diffusing top using a diffusion tensor in its principal coordinate system (PAS) is given by

$$D = \begin{pmatrix} d_{xx} & 0 & 0 \\ 0 & d_{yy} & 0 \\ 0 & 0 & d_{zz} \end{pmatrix} = \begin{pmatrix} d_\perp & 0 & 0 \\ 0 & d_\perp & 0 \\ 0 & 0 & d_\parallel \end{pmatrix} \tag{B.1}$$

is[11,15,42]

$$R_{3,3}^{END} = \frac{2}{45}I(I+1)\sum_p W_{p,p}^{END}\frac{\zeta_p}{1 + (\omega_e\zeta_p)^2} \tag{B.2}$$

where $1/\zeta_p = 6d_\perp + p^2(d_\parallel - d_\perp)$ is the inverse correlation time, τ_c, I is the spin of the nucleus, ω_e is the electron Larmor frequency, and $W_{p,p}^{END}$ is a tensor that accounts for the rotation from the diffusion to A PAS (Ω_{DA}):

$$W^{END} = D^{2\dagger}(W_{DA})\alpha\alpha^\dagger D^2(W_{DA}) \tag{B.3}$$

with

$$\alpha^\dagger = (\alpha_2 \quad \alpha_1 \quad \alpha_0 \quad \alpha_{-1} \quad \alpha_{-2})$$

$$= \sqrt{5}\left(a_- \quad 0 \quad \sqrt{\frac{2}{3}}(a_+ - a_{zz}) \quad 0 \quad a_-\right)$$

and $a_\pm = (a_{yy} \pm a_{xx})/2$.

The CSA relaxation rate is given by

$$R_{3,3}^{CSA} = \frac{1}{25}\sum_p W_{p,p}^{CSA}\frac{\zeta_p}{1 + (\omega_e\zeta_p)^2} \tag{B.4}$$

where ζ_p is the same as before and W^{CSA} is

$$W^{CSA} = D^{2\dagger}(\Omega_{DG})\gamma\gamma^{\dagger}D^2(\Omega_{DG}) \tag{B.5}$$

and

$$\gamma^{\dagger} = \frac{\omega_e\sqrt{5}}{\overline{g}}\left(g_- \quad 0 \quad \sqrt{\frac{2}{3}}(g_+ - g_{zz}) \quad 0 \quad g_-\right)$$

with $g_{\pm} = (g_{yy} \pm g_{xx})/2$ and $\overline{g} = (g_{xx} + g_{yy} + g_{zz})/3$.

Simulations assume that $\Omega_{DG} = \Omega_{DA} = 0$ for simplicity, except in simulations of anisotropic diffusion. In this case, $\Omega_{DG} = \Omega_{DA} = (\pi/2, \pi/2, -\pi)$ in order to align $d_{\parallel}$ with the y-axis. These analytical results neglect electron–nuclear cross-relaxation rates (Overhauser effect) and cross coupling of the END and CSA mechanisms because only the O_0^1 operator is accounted for. A more complete theory presented elsewhere[11] indicates that these terms may be important when the diffusional correlation time (τ_c) and the resonant period ($2\pi/\omega_e$) are of the same order of magnitude.

Expressions for the spin–spin relaxation rates ($R_{4,4} \equiv R_{2e}$) can also be found in the literature.[11] The CSA relaxation rate for the single spin 1/2 particle is given by

$$R_{4,4}^{CSA} = \frac{2}{5}\sigma_{GG}^2\left[\frac{1}{3}J(0) + \frac{1}{4}J(\omega_0)\right] \tag{B.6}$$

where

$$\sigma_{GG}^2 = G_0^2 + 2G_2^2,$$

$$G_0 = \frac{\omega_0}{\overline{g}}\sqrt{\frac{2}{3}}\left[g_{zz} - \frac{1}{2}(g_{xx} + g_{yy})\right],$$

$$\text{and } G_2 = \frac{\omega_0}{\overline{g}}\frac{1}{2}(g_{xx} - g_{yy})$$

The spectral density is given by $J(\omega) = \tau_c/(1 + (\omega\tau_c)^2)$. τ_c is the rotational correlation time.

■ APPENDIX C: IMPLEMENTATION OF SPHERICAL TENSOR FORMALISM

An alternative to solving the equation of motion by evaluating the density matrix elements in terms of a complete set of eigenstates of a secular Hamiltonian is to expand the Hamiltonians and density matrix in terms of the complete set of spherical tensor operators. For each set of eigenstates of total angular momentum j, there corresponds a $(2j + 1)^2$ set of unit spherical tensor operators, $\hat{T}_q^k$, where k and q parallel j and m, respectively. The $\hat{T}_q^k$ are orthonormal in the trace sense:

$$\text{tr}\{\hat{T}_q^k(\hat{T}_{q'}^{\dagger k'})\} = \delta_{k,k'}\delta_{q,q'} \tag{C.1}$$

The operators are $(2j + 1) \times (2j + 1)$ in size and the elements are given by

$$(\hat{T}_q^k)_{m,m'} = (-1)^{k+j+m}\sqrt{2k+1}\begin{pmatrix} j & k & j \\ m' & q & -m \end{pmatrix} \tag{C.2}$$

Spherical tensor operators of an n multispin system are obtained by evaluating the Kronecker product of the operators of each individual spin:

$$\hat{T}_{\mathbf{q}}^{\mathbf{k}} = \hat{T}_{q_1}^{k_1} \otimes \hat{T}_{q_2}^{k_2} \otimes \cdots \otimes \hat{T}_{q_n}^{k_n} \tag{C.3}$$

The observables used in the simulations are expectation values related to the density matrix by means of the expression $O_q^k = \text{tr}\{\hat{T}_q^k\rho\}$. This trace is used to calculate the equilibrium values of the observables since equilibrium is defined in terms of the density matrix as $\rho_0 = e^{-\beta\overline{H}}/\text{tr}\{e^{-\beta\overline{H}}\}$, where $\overline{H}$ is the time-independent Hamiltonian of the system.

The Hamiltonians are in their Liouville form as

$$L = \sum_{k,q} H_q^k \mathcal{L}_q^k \tag{C.4}$$

where

$$H_q^k = \text{tr}\{H\hat{T}_q^{\dagger k}\} \tag{C.5}$$

The H_q^k are scalar quantities that are easily obtained from the Cartesian Hamiltonian, as described below. The $\mathcal{L}$ matrices are of dimension $(2j + 1)^2 \times (2j + 1)^2$ with elements given by

$$(\mathcal{L}_{q_2}^{k_2})_{\binom{k_1}{q_1}\binom{k_3}{q_3}} = \text{tr}\{[\hat{T}_{q_1}^{k_1}, \hat{T}_{q_2}^{k_2}]\hat{T}_{q_3}^{\dagger k_3}\} \tag{C.6}$$

Equation C.6 is also used to evaluate $\mathcal{L}$ for a multispin system, in which case the spherical tensors of eq C.3 are used.

H is constructed directly from the Cartesian spin operators appearing in bilinear terms of the Hamiltonian that take the form $A\mathbf{M}B$, where A and B are two operators (a classical magnetic field operator and a quantum spin operator, or two quantum spin operators) and $\mathbf{M}$ is a coupling tensor. For example, if a nucleus, I, is interacting via the END mechanism with an electron, S, and the electron interacts via the CSA mechanism with the classical externally applied magnetic field, B, then the Hamiltonian is written $H = I_i A_{ij}(t)S_j + B_i(t)G_{ij}(t)S_j$, where $i = x, y, z$ and $j = x, y, z$. (The coherent time dependence in B is included to allow for an oscillating field, and the stochastic time dependence in the A and G tensors is due to the time-dependent rotation from the lab frame of I and S to the PAS of each tensor.)

For a multispin system, the Cartesian components of the operators appearing in the Hamiltonian are formed through the Kronecker product of the individual single spin operators in their matrix representations. These matrices use the single spin basis sets. For example, the matrix representing the product $I_z A_{zz} S_z$ appearing in the END coupling Hamiltonian for a spin 1/2 nucleus, I, interacting with an electron (spin 1/2) requires that appropriate representations of each operator be formed in the larger product space. I_z for this system is calculated as

$$I_z^{\left(\frac{1}{2}\otimes\frac{1}{2}\right)} = I_z^{\left(\frac{1}{2}\right)} \otimes 1_S^{\left(\frac{1}{2}\right)}$$

$$= \begin{pmatrix} -\frac{1}{2} & 0 \\ 0 & \frac{1}{2} \end{pmatrix} \otimes \begin{pmatrix} 1 & 0 \\ 0 & 1 \end{pmatrix}$$

$$= \begin{pmatrix} -\frac{1}{2} & 0 & 0 & 0 \\ 0 & -\frac{1}{2} & 0 & 0 \\ 0 & 0 & \frac{1}{2} & 0 \\ 0 & 0 & 0 & \frac{1}{2} \end{pmatrix} \tag{C.7}$$

where $I_z^{\left(\frac{1}{2}\right)}$ is the 2 × 2 matrix representation of the z component of the nuclear angular momentum operator, and $1_S^{\left(\frac{1}{2}\right)}$ is a unit operator in the space of the electron spin.

Similarly, S_z is given by

$$
S_z^{\left(\frac{1}{2}\otimes\frac{1}{2}\right)} = 1_S^{\left(\frac{1}{2}\right)} \otimes S_z^{\left(\frac{1}{2}\right)}
$$

$$
= \begin{pmatrix} 1 & 0 \\ 0 & 1 \end{pmatrix} \otimes \begin{pmatrix} -\dfrac{1}{2} & 0 \\ 0 & \dfrac{1}{2} \end{pmatrix}
$$

$$
= \begin{pmatrix} -\dfrac{1}{2} & 0 & 0 & 0 \\ 0 & \dfrac{1}{2} & 0 & 0 \\ 0 & 0 & -\dfrac{1}{2} & 0 \\ 0 & 0 & 0 & \dfrac{1}{2} \end{pmatrix}
\tag{C.8}
$$

The bilinear product $I_z A_{zz} S_z$ is therefore

$$
I_z A_{zz} S_z = I_z^{\left(\frac{1}{2}\otimes\frac{1}{2}\right)} A_{zz} S_z^{\left(\frac{1}{2}\otimes\frac{1}{2}\right)} = A_{zz} \begin{pmatrix} \dfrac{1}{4} & 0 & 0 & 0 \\ 0 & -\dfrac{1}{4} & 0 & 0 \\ 0 & 0 & -\dfrac{1}{4} & 0 \\ 0 & 0 & 0 & \dfrac{1}{4} \end{pmatrix}
\tag{C.9}
$$

and this matrix representation is now ready to be used in calculating H_q^k through the trace of a simple matrix multiplication of H with the complete set of $\hat{T}_q^{*k}$ multispin spherical tensor operators as expressed in eq C.5.

APPENDIX D: CALCULATION OF THE EPR SPECTRA

The CW EPR absorption spectrum is calculated as the 1st harmonic of the modulating field used to detect the EPR signal. The nth harmonic has been shown to be equal to[44]

$$
A_n(\Delta) = \frac{1}{2^{\delta_{n,0}}\pi} i^n \int_{-\infty}^{\infty} O_1^1(T) J_n\!\left(\frac{\gamma_e h_m}{2} T\right) e^{-i\Delta T}\, dT
\tag{D.1}
$$

where $O_1^1(T)$ is the transverse magnetization, J_n is the nth order Bessel function, Δ is the Fourier transform frequency, h_m is the modulation field amplitude, and γ_e is the electron gyromagnetic ratio. The spectra illustrated in the results are a plot of the real part of A_1 multiplied by the appropriate phase factor, $e^{i\phi\pi/180}$, where ϕ is the rotation angle in degrees required to correct for the initial pulse that initiates the simulation.

AUTHOR INFORMATION

Corresponding Author
*E-mail: ranged@rpi.edu.

Present Address
§Department of Civil and Environmental Engineering, Rensselaer Polytechnic Institute, Troy, NY 12180, United States.

Notes
The authors declare no competing financial interest.

REFERENCES

(1) Schweiger, A.; Jeschke, G. *Principles of Pulse Electron Paramagnetic Resonance*; Oxford University Press: Oxford, U.K., 2001.

(2) Weil, J. A.; Bolton, J. R. *Electron Paramagnetic Resonance: Elementary Theory and Practical Applications*, 2nd ed.; Wiley-Interscience: New York, 2007.

(3) Abragam, A. *Principles of Nuclear Magnetism*; Oxford University Press: New York, 1983.

(4) Berliner, L. J. *Spin Labeling: Theory and Applications*; Academic Press: New York, 1979.

(5) Berliner, L. J. *Spin Labeling II: Theory and Applications*; Academic Press: New York, 1979.

(6) Berliner, L. J. *Spin Labeling: The Next Millenium*; Springer: New York, 1998.

(7) Brustolon, M.; Giamello, E. *Electron Paramagnetic Resonance: A Practitioners Toolkit*; Wiley: New York, 2009.

(8) Edwards, T. E.; Okonogi, T. M.; Robinson, B. H.; Sigurdsson, S. T. *J. Am. Chem. Soc.* 2001, 123, 1527−1528.

(9) Robinson, B. H.; Mailer, C.; Reese, A. W. *J. Magn. Reson.* 1999, 138, 199−209.

(10) Robinson, B. H.; Mailer, C.; Reese, A. W. *J. Magn. Reson.* 1999, 138, 210−219.

(11) Robinson, B. H.; Reese, A. W.; Gibbons, E.; Mailer, C. *J. Phys. Chem. B* 1999, 103, 5881−5894.

(12) McBride, M. B.; Baveye, P. *Soil Sci. Soc. Am. J.* 1995, 59, 388−394.

(13) Yoshitomi, T.; Suzuki, R.; Mamiya, T.; Matsui, H.; Hirayama, A.; Nagasaki, Y. *Bioconjugate Chem.* 2009, 20, 1792−1798.

(14) Freed, J. H. In *Spin Labeling, Theory and Applications*; Berliner, L. J., Ed.; Molecular Biology, An International Series of Monographs and Textbooks; Academic Press: New York, 1976; Chapter 2.

(15) Mailer, C.; Nielsen, R. D.; Robinson, B. H. *J. Phys. Chem. A* 2005, 109, 4049−4061.

(16) Redfield, A. *IBM J. Res. Dev.* 1957, 1, 19−31.

(17) Smith, A. L.; Cekan, P.; Rangel, D. P.; Sigurdsson, S. T.; Mailer, C.; Robinson, B. H. *J. Phys. Chem. B* 2008, 112, 9219−9236.

(18) Lipari, G.; Szabo, A. *J. Am. Chem. Soc.* 1982, 104, 4546−4559.

(19) Steinhoff, H. J.; Karim, C.; Karim, C. *Ber. Bunsen-Ges., Phys. Chem. Chem. Phys.* 1993, 97, 163−171.

(20) Itzkowitz, M. S. *J. Chem. Phys.* 1967, 46, 3048.

(21) Pedersen, J. *J. Chem. Phys.* 1972, 57, 2680−2683.

(22) Eviatar, H.; van Faassen, E.; Levine, Y. K. *Chem. Phys. Lett.* 1992, 195, 233−238.

(23) Robinson, B. H.; Slutsky, L. J.; Auteri, F. P. *J. Chem. Phys.* 1992, 96, 2609.

(24) Usova, N.; Westlund, P.; Fedchenia, I. I. *J. Chem. Phys.* 1995, 103, 96.

(25) Kubo, R. *J. Phys. Soc. Jpn.* 1969, S26, 1−5.

(26) Håkansson, P.; Westlund, P. O.; Lindahl, E.; Edholm, O. *Phys. Chem. Chem. Phys.* 2001, 3, 5311−5319.

(27) Stoica, I. *J. Phys. Chem. B* 2004, 108, 1771−1782.

(28) Sezer, D.; Sigurdsson, S. T. *Phys. Chem. Chem. Phys.* **2011**, *13*, 12785.

(29) Sezer, D.; Freed, J. H.; Roux, B. *J. Chem. Phys.* **2008**, *128*, 165106.

(30) Rast, S.; Fries, P. H.; Belorizky, E.; Borel, A.; Helm, L.; Merbach, A. E. *J. Chem. Phys.* **2001**, *115*, 7554.

(31) Oganesyan, V. S. *Phys. Chem. Chem. Phys.* **2011**, *13*, 4724.

(32) Oganesyan, V. *J. Magn. Reson.* **2007**, *188*, 196−205.

(33) Håkansson, P.; Nair, P. B. *Phys. Chem. Chem. Phys.* **2011**, *13*, 9578.

(34) DeSensi, S. C.; Rangel, D. P.; Beth, A. H.; Lybrand, T. P.; Hustedt, E. J. *Biophys. J.* **2008**, *94*, 3798−3809.

(35) Budil, D. E.; Sale, K. L.; Khairy, K. A.; Fajer, P. G. *J. Phys. Chem. A* **2006**, *110*, 3703−3713.

(36) Beier, C.; Steinhoff, H. *Biophys. J.* **2006**, *91*, 2647−2664.

(37) Aman, K.; Westlund, P. *Phys. Chem. Chem. Phys.* **2007**, *9*, 691−700.

(38) Steinhoff, H.; Hubbell, W. *Biophys. J.* **1996**, *71*, 2201−2212.

(39) Oganesyan, V. S.; Kuprusevicius, E.; Gopee, H.; Cammidge, A. N.; Wilson, M. R. *Phys. Rev. Lett.* **2009**, *102*, 013005.

(40) Usova, N.; Persson, L.; Westlund, P. *Phys. Chem. Chem. Phys.* **2000**, *2*, 2785−2793.

(41) Nielsen, R. D.; Robinson, B. H. *J. Phys. Chem. A* **2004**, *108*, 1589−1600.

(42) Hubbard, P. S. *Phys. Rev.* **1963**, *131*, 1155.

(43) Robinson, B.; Haas, D.; Mailer, C. *Science* **1994**, *263*, 490−493.

(44) Nielsen, R. D.; Hustedt, E. J.; Beth, A. H.; Robinson, B. H. *J. Magn. Reson.* **2004**, *170*, 345−371.

(45) Owenius, R.; Eaton, G. R.; Eaton, S. S. *J. Magn. Reson.* **2005**, *172*, 168−175.

(46) Berliner, L. J. *In Vivo EPR (ESR): Theory and Applications*, 1st ed.; Springer: New York, 2003.

(47) Eaton, G. R.; Eaton, S. S.; Ohno, K. *EPR Imaging and In Vivo EPR*, 1st ed.; CRC Press: Boca Raton, FL, USA, 1991.

(48) Yokoyama, H. *EPR Imaging and Its in vivo Application*, 1st ed.; Nova Science Publishers: Hauppauge, NY, USA, 2009.

(49) Nielsen, R. D.; Robinson, B. H. *Concepts Magn. Reson., Part A* **2006**, *28A*, 270−290.

(50) Harriman, J. E. *Theoretical Foundations of Electron Spin Resonance*; Physical Chemistry 37; Academic Press: New York, 1978.

(51) Golub, G. H.; Van Loan, C. F. *Matrix Computations*, 3rd ed.; Johns Hopkins Studies in Mathematical Sciences; The Johns Hopkins University Press: Baltimore, MD, USA, 1996.

(52) Higham, N. J. *SIAM Rev.* **2009**, *51*, 747.

(53) Moler, C.; Loan, C. V. *SIAM Rev.* **1978**, *20*, 801.

(54) Wang, D.; Hanson, G. R. *J. Magn. Reson., Ser. A* **1995**, *117*, 1−8.

(55) Ponti, A. *J. Magn. Reson.* **1999**, *138*, 288−297.

(56) Edén, M. *Concepts Magn. Reson., Part A* **2003**, *17A*, 117−154.

(57) Edén, M. *Concepts Magn. Reson., Part A* **2003**, *18A*, 24−55.

(58) Edén, M. *Concepts Magn. Reson., Part A* **2003**, *18A*, 1−23.

(59) Karney, C. F. *J. Mol. Graphics Modell.* **2007**, *25*, 595−604.

(60) Matubayasi, N.; Nakahara, M. *J. Chem. Phys.* **1999**, *110*, 3291−3301.

(61) Matsumoto, M.; Nishimura, T. *ACM Trans. Model. Comput. Simul. (TOMACS)* **1998**, *8*, 3−30.

(62) Levenberg, K. *Q. Appl. Math.* **1944**, *2*, 164−168.

(63) Marquardt, D. W. *J. Soc. Ind. Appl. Math.* **1963**, *11*, 431−441.

(64) Press, W. H.; Teukolsky, S. A.; Vetterling, W. T.; Flannery, B. P. *Numerical Recipes: The Art of Scientific Computing*, 3rd ed.; Cambridge University Press: Cambridge, U.K., 2007.

(65) Nielsen, R. D.; Canaan, S.; Gladden, J. A.; Gelb, M. H.; Mailer, C.; Robinson, B. H. *J. Magn. Reson.* **2004**, *169*, 129−163.

(66) Hubbard, P. S. *Phys. Rev. A* **1974**, *9*, 481.